

EXPERIMENTS AND MODELING OF THE EFFECTS OF HEAT  
EXPOSURE ON FATIGUE OF 6061 AND 7075  
ALUMINUM ALLOYS

by

ANDREW THOMAS BRAMMER

J. BRIAN JORDON, COMMITTEE CHAIR  
MARK E. BARKEY  
BETH TODD

A THESIS

Submitted in partial fulfillment of the requirements for the degree of  
Master of Science in the Department of Mechanical Engineering  
in the Graduate School of The University of Alabama

TUSCALOOSA, ALABAMA

2013

Copyright Andrew Thomas Brammer 2013  
ALL RIGHTS RESERVED

## ABSTRACT

Strain-controlled fatigue tests were performed on 6061-T6 and 7075-T651 aluminum alloys as well as additional specimens of the same materials after exposure to a temperature of 538°C for 1 hour and cooling to room temperature. The fatigue behavior of all four materials was characterized using traditional strain-life analysis. The fatigue data was found to show no appreciable effect of the heat exposure in low cycle fatigue, and a decrease in fatigue life in high cycle fatigue in both 6061 and 7075. In addition, scanning electron microscopy was employed to determine that crack initiation occurred at Fe-rich particles and subsequent analysis was used to measure crack growth rates. The fatigue cracks were found to initiate at cracked intermetallic particles in the peak-aged alloys and at de-bonded particles in the heat exposed alloys. Using standard metallographic techniques, microstructural characterization including grain size, intermetallic particle size, and nearest neighbor distance were quantified. As such, this characterization data was implemented into a microstructure-sensitive fatigue model resulting in a unique set of modeling parameters to capture the experimental results of both the peak-aged and thermally-affected 6061 aluminum alloy and 7075 aluminum alloy data.

## DEDICATION

This thesis is dedicated to all of my family and friends who have been providing moral support throughout the time I have been working on this study.

## LIST OF ABBREVIATIONS AND SYMBOLS

$C_m$	Coefficient in Modified Coffin Manson Law
$\alpha$	Ductility exponent in Modified Coffin Manson Law
$q$	Exponent in remote strain to local plastic shear strain
$y_1$	Constant in remote strain to local plastic shear strain
$y_2$	Linear constant in remote strain to local plastic shear strain
$\xi$	Geometric factor in micromechanics study
$r$	Exponent in micromechanics study
$\omega$	Omega
$\sigma$	Load path dependent and loading combination parameter
$\zeta$	Exponent in small crack growth
$C_I$	HCF constant in small crack growth
$C_{II}$	LCF constant in small crack growth
$\chi$	Crack growth rate constant
$\varepsilon_f'$	Fatigue ductility exponent

$\sigma_f'$	Fatigue strength coefficient
b	Fatigue strength exponent
c	Fatigue ductility exponent
N	Fatigue life in cycles
$\Delta\varepsilon_e/2$	Elastic strain range
$\Delta\varepsilon_p/2$	Plastic strain range
K'	Cyclic strength coefficient
n'	Cyclic strain hardening exponent
MSF	Multistage Fatigue

## ACKNOWLEDGEMENTS

I would like to thank everyone who helped me to be able to complete this degree, to enumerate: Dr. Jordon, for guidance, Dr. Todd, for allowing me to participate in the GK-12 program, and Dr. Barkey, for sharing his expertise in material testing through class and helping me learn to conduct tests in a research setting. Additionally, I would like to thank Johnny Godwin and Rich Martens in the Central Analytical Facility for the University of Alabama for teaching me to use the scanning electron microscopes for imaging, EDS, and EBSD. Finally, I would like to thank some other graduate students who helped me learn how to use various pieces of equipment along with helping me make sure I was on top of all of the requirements: Harish Rao, Todd Butler, Dave Metz, and Ousama Abdelhadi.

## CONTENTS

ABSTRACT.....	ii
DEDICATION.....	iii
LIST OF ABBREVIATIONS AND SYMBOLS.....	iv
ACKNOWLEDGEMENTS.....	vi
LIST OF TABLES.....	ix
LIST OF FIGURES.....	x
1. Introduction.....	1
2. Experiment.....	4
2.1. Materials and Specimens.....	4
2.2. Experimental Procedure.....	4
3. Fatigue Model.....	6
3.1. Strain-Based Approach.....	6
3.2. Microstructure-Based Approach.....	7
3.2.1. Stages of Fatigue Damage.....	8

3.2.2. Crack Incubation Regime.....	8
3.2.3. Small Crack Growth Regime.....	10
3.2.4. Long Crack Growth Regime.....	11
4. Results and Discussion.....	12
4.1. Microstructure.....	12
4.2. Monotonic Stress-Strain Behavior.....	13
4.3. Cyclic Stress-Strain Behavior.....	13
4.4. Fatigue Crack Initiation.....	15
4.5. Fatigue Crack Growth.....	16
4.6. Multistage Fatigue Model Correlations.....	17
5. Summary.....	19
6. References.....	21

## LIST OF TABLES

1. Monotonic Properties of 6061-T6, 6061-A, 7075-T651, and 7075-A.....	24
2. List of tested specimens, including cycles to failure and strain amplitude ( * indicates runout).....	25
3. Cyclic Properties of 6061-T6, 6061-A, 7075-T651, and 7075-A.....	27
4. Multistage Fatigue (MSF) Model constants.....	28

## LIST OF FIGURES

1. The intermetallic particles of a) 6061-T6, b) 6061-A, c) 7075-T651, and d) 7075-A aluminum alloys.....	29
2. Histogram of the area of individual intermetallic particles for a) 6061 and b) 7075 aluminum alloys.....	30
3. The etched microstructure of a) 6061-T6, b) 6061-A, c) 7075-T651, and d) 7075-A aluminum alloys.....	32
4. The monotonic and cyclic stress strain curves for a) 6061 and b)7075 aluminum alloys.....	33
5. The strain-life equation fits for a) 6061 and b) 7075 aluminum alloys.....	35
6. The first cycle hysteresis loops for the a) 6061-T6, b) 6061-A, c) 7075-T651, and d) 7075-A aluminum alloys.....	37
7. Stabilized (mid-cycle) hysteresis cycles for a) 6061-T6, b) 6061-A, c) 7075-T651, and d) 7075-A aluminum alloys.....	41
8. Stress-amplitude evolution over the cycle of the fatigue test for a) 6061-T6, b) 6061-A, c) 7075-T651, and d) 7075-A aluminum alloys.....	45
9. The particle in the image of specimen T-6-5, tested at 0.003 strain amplitude, is typical of the crack initiation sites found in the 6061-T6 aluminum alloy.....	49

10. The particle in this image specimen A-6-10, tested at 0.007 strain amplitude is typical of the crack initiation sites in the 6061-A aluminum alloy, with clusters of particles that are larger than those found in the 6061-T6 aluminum alloy.....	50
11. The particle in this image of specimen T-7-20, tested at 0.0045 strain amplitude is indicative of the initiation sites of 7075-T651. Almost exclusively the failures occurred at particle clusters.....	51
12. The particle in this image of specimen A-7-1 tested at 0.007 strain amplitude is one of the typical modes of failure.....	52
13. Fatigue striations were seen on most fracture surfaces on all materials represented by these shown from specimen A-6-8, with the crack growth direction indicated by the arrow.....	53
14. Compiled crack growth rates respective to overall crack length for a) the 6061 aluminum alloy and b) the 7075aluminum alloy.....	54
15. MSF model fit to the strain-controlled fatigue data in the peak-aged and heat-effected states for a) AA6061 and b) AA7075 aluminum alloys.....	56
16. MSF fit of incubation and small crack growth for a) 6061-T6, b) 6061-A, c) 7075-T651, and d) 7075-A aluminum alloys.....	58

## 1. Introduction

Since most structural components fail due to cyclic loading, the capability to accurately predict the structural health of a component under expected and unexpected conditions is paramount to safe designs. In the aerospace and automotive industries interested in lightweight designs, aluminum alloys are frequently used as structural and sheeting components. As such, there are several common high-strength aluminum alloys that are typically used, including many of the 2XXX, 6XXX, and 7XXX series aluminum alloys. In fact, the 6061 aluminum alloy is one of the most easily formable of this group of aluminum alloys but does not offer high strength, whereas, the 7075 aluminum alloy is typically employed for its high strength. The 6061 is an aluminum-silicon-magnesium alloy that has good strength and very high formability that allows it to be extruded or otherwise formed into complex geometries like multi-hollow bodies [1]. This makes aluminum 6061-T6 aluminum alloys very adaptable for use in the form of plates, extrusions, foils, sheets, pipes, forgings, and even structural forms in the aerospace, construction, and transportation industries [2]. On the other hand, the 7075 is an aluminum-zinc alloy that has a higher specific strength but a lower formability. This lower formability limits its use to structural members in less complicated geometries (rolled plates) especially in the aerospace and transportation industries [1].

As many components and structures employ aluminum alloys like 6061 and 7075 in order to reduce weight while maintaining strength, there are some unexpected consequences in applications involving exposure to medium to high temperatures. In fact, the effect of high

temperature exposure approaching annealing conditions on the fatigue behavior of some common aluminum alloys merits further examination. Recent work by Prietto et al. [3] showed high-temperature degradation of tensile behavior in a 6061-T6 aluminum alloy subjected to a thermal blast. Here, the material exposed to higher temperatures had both a lower hardness and a lower tensile strength. In addition, the effect of heat treatment on the monotonic mechanical properties of 6061 aluminum was also explored by Mrówka-Nowotnik [4], where variation of Young's Modulus (E), strength coefficient (K), strain-hardening exponent (n), and hardening coefficient (m), were quantified with respect to the aging time. The strength coefficient value was found to increase with aging beyond the T6 temper, but the strain-hardening exponent and hardening exponent values decreased while Young's Modulus stayed relatively constant.

Unlike in the case of 6061 aluminum alloy, the effect of high temperature exposure on the fatigue properties of 7075-T651 aluminum alloy have not been studied directly; however, the effect of annealing on monotonic and anisotropy in cold worked 7075 aluminum alloy[5] was studied. Annealing at 400°C for 5 minutes provided for the optimal forming characteristics and anisotropy [5]. As such, the effect of annealing or high temperature exposure on fatigue strength or fundamental mechanism is not understood.

In traditional fatigue analysis, an empirical curve fit is applied to load-controlled or strain-controlled cyclic experimental data to generate fatigue properties that can be used correlate the general trends expected from a given material. However, fatigue data commonly has scatter up to an order of magnitude in fatigue lives that cannot be captured by these classical methods accurately due to the nature of a curve fit. Furthermore, any change in the material or temper necessitates a re-characterization of the "new" material and model fitting without a direct link to the underlining mechanism. Thus, to address this, a multistage engineering fatigue model was

proposed by McDowell, et al. [6], to address effects of different microstructure features and defects in cast aluminum alloys. This model has since been expanded to wrought aluminum alloys, magnesium alloys, and some steel alloys [7-15]. The multistage fatigue model discretizes the fatigue process into experimentally observed stages including as crack incubation (inc), microstructurally small crack growth (MSC), physically small crack growth (PSC), and long crack growth (LC) [6]. This model employs microstructural information and macroscopic material properties to account for variation fatigue life, fatigue data scatter, and the contribution of the different phases of the fatigue process. As such, the purpose of this paper is to explore the effect of high-temperature exposure on the fatigue behavior of 6061 and 7075 aluminum alloys and use the multistage fatigue modeling paradigm to capture the trends from both the peak-aged and heat-affected alloys under fully-reversed applied cyclic loading.

## **2. Experiment**

### *2.1. Materials and Specimens*

The 6061-T6 and 7075-T651 aluminum alloys were obtained in an extruded form and machined into dog-boned shaped fatigue specimens following ASTM E606 [17] that contained a 13 mm gage length. Both the 6061 and 7075 aluminum alloy specimens were divided into two groups, one group was tested in the as received condition, while the second group was tested after exposure to a temperature of 538°C for 1 hour and then cooled to room temperature prior to testing. For the purposes of this paper, the temperature exposed material will be referred to as annealed and designated as 6061-A and 7075-A, respectively. Prior to being loaded in the testing machine all of these specimens were hand-ground in the axial direction with 800 grit metallurgical paper to remove any circumferential marks due to machining.

### *2.2. Experimental Procedure*

To examine the microstructure of the two aluminum alloys, untested specimens were sectioned in both the cross section and extruded direction. A compression mounted phenolic epoxy was applied prior to grinding and polishing to a 1 $\mu$ m finish and a Keller's etchant was used to etch the materials. The grain sizes were calculated using the intercept method according to ASTM E112 [17]. Using an optical microscope, the statistical size and nearest neighbor distance of intermetallic particles were quantified. Furthermore, a computer-based image-

analyzer, originally employed in [16], was used to measure the statistical information from the images on the microstructural features like particle size and spacing.

Monotonic tests were conducted at a strain rate of 0.0001mm/mm/s to failure and the strain was measured using an axial extensometer with a 12.5mm gage length. The fatigue tests were performed using an axial extensometer under strain control at 5 Hz under fully reversed ( $R = -1$ ) loading to 50,000 cycles. Note that under strain control, the load was allowed to develop during each cycle. After 50,000 cycles, the specimen was considered cyclically stable and the tests were continued to failure in load control at 30 Hz. Strain amplitudes tested were 0.002, 0.003, 0.004, 0.005, 0.006, and 0.007 with the 7075-T651 also being tested at 0.008 and 0.009 strain amplitudes to achieve appreciable plasticity for modeling purposes. Failure of the strain fatigue tests was defined as a 50% drop in the peak stress amplitude achieved.

The fracture surfaces from the fatigue tests were examined using scanning electron microscopy (SEM) for the purposes of measuring crack growth striations and identifying crack initiation sites. The specimens were prepared by cutting immediately below the fracture surface, mounting to an SEM sample holder using carbon tape, and cleaning in a plasma cleaner for 5:00 minutes. An Electron Diffraction Spectroscopy (EDS) Camera was used to gather chemical analysis of the initiation sites in the fracture surfaces.

### 3. Fatigue Model

#### 3.1 Strain-Based Approach

Strain-based fatigue modeling is used frequently in low-cycle fatigue applications where it can accurately capture the plasticity driving fatigue damage in this regime. The strain-based approach works using a fully-reversed, constant-amplitude test to resolve elastic and plastic strains, as shown in Equation 2.

$$\Delta\varepsilon = \Delta\varepsilon_e + \Delta\varepsilon_p \quad (2)$$

The stress amplitude,  $\Delta\sigma/2$ , can be expressed as a function of the number of reversals empirically by the Basquin equation [18-21]

$$\frac{\Delta\sigma}{2} = \sigma'_f (2N_f)^b \quad (3)$$

where  $\sigma'_f$  is the fatigue strength coefficient and  $b$  is the fatigue strength exponent. Since the elastic strain amplitude,  $\Delta\varepsilon_e$ , is equal to  $\Delta\sigma/2 E$ , where  $E$  is the elastic modulus, Eq. (3) can be transformed to give the elastic strain amplitude as

$$\frac{\Delta\varepsilon_e}{2} = \frac{\sigma'_f}{E} (2N_f)^b \quad (4)$$

On the other hand, the dependence of reversals to failure on the plastic strain amplitude is represented by the Coffin-Manson equation [18-21]

$$\frac{\Delta\varepsilon_p}{2} = \varepsilon'_f (2N_f)^c \quad (5)$$

where  $\varepsilon'_f$  is the fatigue ductility coefficient, and  $c$  is the fatigue ductility exponent. Combining Eqs. (3) and (4), we obtain the total strain amplitude as a function of the number of cycles to failure [18-21]

$$\frac{\Delta\varepsilon}{2} = \frac{\sigma'_f}{E} (2N_f)^b + \varepsilon'_f (2N_f)^c \quad (6)$$

Similar to monotonic stress-strain curves that have been used to determine design parameters for engineering structures and components, cyclic stress-strain curves can be used to assess the durability of the same structures and components which experience cyclic loading. Analogous to the monotonic deformation in tension, the cyclic stress-strain behavior can be represented by a power law function [20]

$$\frac{\Delta\sigma}{2} = K' \left( \frac{\Delta\varepsilon_p}{2} \right)^{n'} \quad (7)$$

where  $K'$  is the cyclic strength coefficient and  $n'$  is the cyclic strain hardening exponent.

### 3.2 Microstructure-Based Approach

The Multistage fatigue (MSF) model was originally developed to model a cast Al-Si-Mg alloy [6], and it has since been expanded to model wrought aluminum alloy [7-9,12], cast magnesium alloys [10, 13-14], and wrought magnesium alloys [15, 21]. In this model, the number of cycles are associated with the specific stages of damage are given below:

$$N_{total} = N_{inc} + N_{MSC} + N_{PSC} + N_{LC} = N_{inc} + N_{MSC/PSC} + N_{LC} \quad (1)$$

where  $N_{inc}$  is the number of cycles to incubate a crack at a micronotch that includes the nucleation of crack-like damage and early crack propagation through the zone of the micronotch's root influence;  $N_{MSC}$  is the number of cycles required for propagation of a

microstructurally small crack;  $N_{PSC}$  is the number of cycles required for propagation of a physically small crack (PSC), and  $N_{LC}$  is the number of cycles required for long crack propagation.

### 3.2.1. Stages of Fatigue Damage

Crack incubation involves nucleation plus small crack growth at the micronotch on the order of  $\frac{1}{2} D$ , where  $D$  is the inclusion size. Small crack growth (MSC) comprises propagation of microstructural cracks with lengths that fall within  $a_i < a < k MS$ , where  $a_i$  is the initial crack length,  $MS$  is a characteristic length scale (defined as the smallest grain size) of interaction with microstructural (MS) features, and  $k$  is a multiplier where  $1 \leq k \leq 3$  [6-7]. The PSC range consists of crack propagation with a crack length in the interval of  $k MS < a < \sim (10 MS)$ . Depending on the microstructural inclusion morphology and texture of the matrix, the PSC regime may extend from 300  $\mu\text{m}$  to  $\sim 2\text{-}3$  mm in length.

### 3.2.2. Crack Incubation Regime

The fatigue damage incubation life,  $N_{inc}$ , is characterized by the cyclic damage at the micronotch root. For the purposes of this paper the terms micro-notch and inclusion are used interchangeably. This required implementation of a modified Coffin-Manson law [6] at the microscale as follows:

$$C_{inc} N_{inc}^{\alpha} = \beta = \frac{\Delta\gamma_{max}^{p*}}{2} \quad (8)$$

where  $\beta$  is the nonlocal damage parameter around an inclusion,  $\frac{\Delta\gamma_{max}^{p*}}{2}$  is the local average maximum plastic shear strain amplitude, and  $C_{inc}$  and  $\alpha$  are linear and exponential coefficients for fatigue crack incubation life, respectively. The numerical value of the exponent  $\alpha$  was

selected to be in the range of the macroscopic Coffin-Manson law [6]. Note that  $\beta$  is estimated by the following relations:

$$\beta = \frac{\Delta\gamma_{max}^{p*}}{2} = Y[\varepsilon_a - \varepsilon_{th}]^q, \quad \frac{l}{D} < \eta_{lim}, \quad (9)$$

$$\beta = \frac{\Delta\gamma_{max}^{p*}}{2} = Y(1 + \zeta \frac{l}{D})[\varepsilon_a - \varepsilon_{th}]^q, \quad \frac{l}{D} > \eta_{lim}. \quad (10)$$

Here,  $\varepsilon_a$  is the remote applied strain amplitude,  $\varepsilon_{th}$  is the microplasticity threshold, and  $l$  is the nominal linear dimension of the plastic zone size in front of the inclusion. The ratio  $\frac{l}{D}$  is defined as the square root of the ratio of the plastic zone over the inclusion area, and the parameters  $q$  and  $\zeta$  are determined from micromechanical simulations [7]. The limiting ratio,  $\eta_{lim}$ , indicates the transition from proportional (constrained) micronotch root plasticity to nonlinear (unconstrained) micronotch root plasticity with respect to the applied strain amplitude, where  $\eta_{lim} = 0.3$  has been found to be suitable for extruded Al alloys. [7]. Future micromechanical finite element simulations will be needed to confirm that this limiting ratio is the same for all four materials. The parameter  $Y$  [6-7] is correlated as  $Y = y_1 + (1 + R)y_2$ , where  $R$  is the load ratio, and  $y_1$  and  $y_2$  are model constants. For completely reversed loading cases,  $Y = y_1$ .

Furthermore, when  $\frac{l}{D}$  reaches its limits the parameter  $Y$  is revised to include the geometric effects related to the type of inclusion,  $\bar{Y} = (1 + \frac{l}{D})Y$ . The debonded particle and pore of the same size may cause a different  $Y$  as a factor of three or greater [23]. The correlation of the plastic zone size is calculated using the  $\frac{\Delta\gamma_{max}^{p*}}{2}$  with respect to the remote loading strain amplitude,

$$\frac{l}{D} = \eta_{lim} \frac{\langle \varepsilon_a - \varepsilon_{th} \rangle}{\varepsilon_{per} - \varepsilon_{th}}, \quad \frac{l}{D} \leq \eta_{lim}, \quad (11)$$

$$\frac{l}{D} = 1 - (1 - \eta_{lim}) \left( \frac{\varepsilon_{per}}{\varepsilon_a} \right)^r, \quad \frac{l}{D} > \eta_{lim}, \quad (12)$$

where  $r$ , a shape constant for the transition to the limited plasticity, is determined through micromechanical simulations [7], and  $\varepsilon_{per}$  is the percolation limit [6].

### 3.2.3 Small Crack Growth Regime

Similar to modeling efforts in wrought Al alloys [7], we combine the mathematical expressions for the MSC and PSC regimes into a single mathematical form. Crack growth in the MSC/PSC is governed by the range of crack tip displacement,  $\Delta CTD$ , which is proportional to the crack length, and the  $n^{\text{th}}$  power of the applied stress amplitude,  $\sigma_a^n$ , in the high cycle fatigue (HCF) regime and to the macroscopic plastic shear strain range,  $\frac{\Delta \gamma_{max}^P}{2}$ , in the low cycle fatigue (LCF), and it is given by the following,

$$\left( \frac{da}{dN} \right)_{MSC} = \chi (\Delta CTD - \Delta CTD_{th}), \quad a_i = 0.625D \quad (13)$$

$$\Delta CTD = C_{II} \left( \frac{GS}{GS_0} \right)^\omega \left[ \frac{U \Delta \hat{\sigma}}{S_{ut}} \right]^\zeta a_i + C_I \left( \frac{GS}{GS_0} \right)^\omega \left( \frac{\Delta \gamma_{max}^P}{2} \right)^2 \quad (14)$$

Here,  $\chi$  is a constant for a given microstructure, typically less than unity and usually taken as 0.32 for several different alloys [7],  $a_i$  is the initial crack length,  $GS$  is grain size,  $GS_0$  is a reference grain size. The  $C_I$ ,  $C_{II}$ , and  $\chi$  are material dependent parameters that capture the microstructural effects on MSC growth [6-8]. The threshold value for crack tip displacement was defined on the order of the Burger's vector for the Al-rich matrix [24],  $\Delta CTD_{th} = 3.2 * 10^{-4} \mu m$ . The term  $\Delta \hat{\sigma}$  is the combination of the uniaxial effective stress amplitude,  $\bar{\sigma}_a =$

$\sqrt{\frac{3}{2} \frac{\Delta \sigma'_{ij}}{2} \frac{\Delta \sigma'_{ij}}{2}}$ , and the maximum principal stress range,  $\Delta \sigma_1$ , and is given as  $\Delta \hat{\sigma} = 2\theta \bar{\sigma}_a + (1 -$

$\theta)\Delta\sigma_1$ , with  $0 \leq \theta \leq 1$  as the path dependent loading parameter after Ref. [7], where  $\theta$  is a weighting parameter such that  $\theta = 0$  gives the von Mises stress state, and  $\theta = 1$  gives the maximum for principal stress state. The parameter  $U$  is employed to incorporate the load ratio effects and is defined as  $U = \frac{1}{1-R}$  [7]. To capture the effect of grain size on small crack growth, we employ the ratio of grain size to the reference size  $\left(\frac{GS}{GS_0}\right)^\omega$  for each of the three materials in this study, where  $GS_0$  is the reference grain size,  $GS$  is the specific grain size, and  $\omega$  is a material parameter [6].

### *3.2.4 Long Crack Growth Regime*

The long crack growth stage of the MSF model usually follows classical linear elastic fracture mechanics (LEFM) approaches [6]. The model approach used in this study uses only the incubation and MSC/PSC regimes, like Jordon et al. [12], which has been shown capable of characterizing cracks up to several millimeters in length [6]. Thus, the MSF model is essentially used to predict the onset of surface crack initiation in structural components and therefore long crack propagation is generally not considered.

## 4. Results and Discussion

### 4.1. Microstructure

The intermetallic particles were observed through optical microscopy of polished specimens, and the images are shown in Figure 1. The intermetallic particles present in 7075-T651 aluminum alloy are primarily either  $MgZn_2$ , which appear very dark under an optical microscope, or Fe-rich particles, which appear as an intermediate color between the  $MgZn_2$  and the base material. From Agarwal et al. [25], the 6061 aluminum alloy shows the same color tendencies with  $Mg_2Si$  particles in place of the as the 7075 aluminum alloy. Particles stringers were observed in the 7075 aluminum alloy in the direction of extrusion direction but were not present in the 6061 aluminum alloy. Furthermore, the particle alignment in the 6061 aluminum alloy exhibited no orientation preference relative to the extrusion direction. The particle sizes are also shown graphically in the histogram, in Figure 2, which shows that the 7075 aluminum alloys have more total particles, and the 6061 aluminum alloy has a higher concentration of larger particles. In both materials, the high-temperature exposure increased the total number of particles visible under 1000x optical magnification, and an increase in particle size was also observed. In addition, a nominal intermetallic particle size and nearest neighbor distance were determined for each of the materials, and since the Fe-rich particles are the typical crack initiation site in all of these materials, the statistical bound of the particle size can be combined with the MSF model to predict the scatter of the fatigue data. The etched granular structure for all four materials are

presented in Figure 3. The 6061-T6 aluminum alloy was found to have a grain size of around 75 $\mu\text{m}$ , and the 7075-T651 aluminum alloy was found to have a nominal grain size of 105 $\mu\text{m}$ .

#### *4.2. Monotonic Stress-Strain Behavior*

The monotonic tensile behavior of these aluminum alloys was examined and characterized prior to fatigue testing. The monotonic tensile curves can be seen in Figure 4 with the cyclic stress-strain curve. In comparing the peak-aged and heat-exposed specimens, the elastic components are almost identical, with very little difference in elastic modulus, but both 6061-A and 7075-A aluminum alloys exhibit significant decreases in yield and ultimate strength. Specifically, the yield strength decreased approximately 50% in the heat-affected specimens, and the ultimate strength decreased by approximately 33%. These results compare closely to work by Prietto et al. [3] where similar decreases in the strength of 6061 aluminum alloy were observed, including a loss of strength and decrease in hardness. This decrease in mechanical properties is due to a thermal-resetting of the work-hardening present in the T6 and T651 tempers. This conclusion is supported by comparison to the stabilized cyclic stress-strain curves, where the 7075-T651 shows no strain hardening, while the 6061-T6 shows appreciable strain-hardening at higher strain amplitudes. However, the cyclic 6061-A more closely follows the monotonic 6061-T6 curve, and the 7075-A curve shows significant strain hardening, although it does not approach the monotonic level of 7075-T651. Table 1 shows the monotonic characterization of all 4 specimen sets, which indicates that both the 7075 aluminum alloys have a higher yield and ultimate strength than the corresponding 6061 aluminum alloys.

### 4.3. Cyclic Stress-Strain Behavior

The strain-life experimental results are shown in Figure 5 along with the strain-based modeling approach. The strain-life approach provides a good representation of the experimental trends of both the peak-aged and heat degradation effects. The experimental results for both 6061 and 7075 aluminum alloys show similar trends, whereas during low cycle fatigue (LCF) no appreciable difference was observed between the peak aged and heat-affected materials. This lack of difference is due to an increase in ductility compensating for a loss in yield and ultimate strength in the heat-affected aluminum alloy. However, in high cycle fatigue (HCF), however, both materials show significant degradation in number of cycles to failure in the heat-exposed aluminum alloys due to the lower yield and ultimate strengths when compared to the peak-aged aluminum alloys. In the 6061-A at HCF, the plastic strain contribution is nearly twice as large as in the T6 temper. By contrast, in the 7075 aluminum alloys, the T651 temper is almost exclusively captured by the elastic portion of the strain life equation, while the annealed condition shows a significant contribution of the plastic strain component above a strain amplitude of 0.004. Table 2 shows a list of all specimens tested, including the specific strain-levels tested at and cycles to failures.

In Figure 6, the hysteresis response from the first cycle is shown. The hysteresis loops show a significantly larger amount of plasticity in the heat-exposed specimens as opposed to the T6 specimens in both the 6061 aluminum alloy and T651 in the 7075 aluminum alloy. Figure 7 shows the cyclically stable hysteresis response, which illustrates that some plasticity is still present at all strain amplitudes except for the 7075-T651 aluminum alloy. Note, the 6061-A and 7075-A do not achieve a cyclically stable state, so the cycle prior to load drop off was used in plotting Figure 7. Figure 8 shows the stress amplitude versus number of cycles for the 6061 and

7075 aluminum alloys. From Figure 8b and 8d it is apparent that the cyclic hardening is most pronounced in the 6061-A and 7075-A specimens, and is only present in the highest strain amplitude tests in the 7075-T651. The difference between the peak aged and heat effected materials is due to a thermal-resetting of the work hardening in the T6/T651 specimens during the "annealing" process.

#### *4.4. Fatigue Crack Initiation*

In both materials, the dominant fatigue crack that lead to fracture was found to have typically initiated and propagated through a flat area on the fracture surface. The fatigue cracks were found to initiate at Fe-rich particles in both 6061-T6 and 7075-T651 aluminum alloys similarly observed elsewhere [7-9,12,25]. Based on SEM analysis, the 6061-T6 aluminum alloys was observed to fail primarily due to particle cracking and crack propagation similar to observations reported by Agarwal et al. [25]. A representative fracture surface for the 6061-T6 aluminum alloy tested at 0.003 strain amplitude is shown in Figure 9 where the particle that initiated the fatigue crack is outlined. Figure 10 shows a representative fracture surface from 6061-A tested at 0.007 strain amplitude. Typically, the initiation site revealed particles that are larger than the statistical mean particle size. Additionally, particle de-bonding was observed more frequently in the annealed aluminum alloy than the T6 version, likely due to the decrease in yield/ultimate strength seen in the annealed aluminum alloy. Based on the particle size analysis shown in Figure 2, this disparity in initiating particle size and the higher frequency of particle clusters at initiation sites are likely due to the increase in the number of particles of all sizes in 6061-A compared to 6061-T6.

The 7075-T651 aluminum alloy was found to initiate cracks primarily at intermetallic particle stringers through particle cracking similar to reported elsewhere [7-9,12]. A representative initiation site for the 7075-T651 aluminum alloy is shown in Figure 11 for a specimen tested at a strain amplitude of 0.0045. Several particles that all initiated cracks are clearly illustrated on the top edge of the specimen. The most common mode of crack initiation was particle cracking as reported by Xue et al. [7-9]. Similarly, Figure 12 shows a typical initiation site for 7075-A tested at a strain amplitude of 0.007. It was observed that fatigue cracks initiated at both particle clusters and individual particles due to particle cracking primarily. However, some particle debonding was observed but not as frequently as in the 6061-A aluminum alloy.

#### *4.5. Fatigue Crack Growth*

Figure 13 shows a representative image of the striations area approximately 0.05 mm from the initiation location of a 6061-A specimen tested at a strain amplitude of 0.007. The distance at which the striations were discernible from the initiating particle varied from 50  $\mu\text{m}$  to 150  $\mu\text{m}$ , and particularly with the 7075-T651, interactions between striations from multiple initiation sites typically limited measurements outside of certain regions. The crack growth rate is related to the width of the fatigue striations, and the correlation between the crack growth rate and overall crack length is shown in Figure 14. Some scatter is observed in Figure 14, but the crack growth rate suggests an upward trend as the crack propagates through the specimen. By comparing the peak aged specimens to the heat-degraded samples, the crack growth rate increased at a slower rate with respect to crack length in the peak aged specimens. Furthermore, the peak aged aluminum alloy is more resistant to crack propagation for any given overall crack length. Additionally, the scatter observed in the striation results plotted in Figure 14 is caused by

multiple factors, including low-angle grain boundaries and intermetallic particles impeding the crack growth, but the overall increasing crack growth rate is observed. The difference in crack growth rates between the peak aged and heat exposed aluminum alloys is most notably caused by the decrease in yield and ultimate strength. This decrease in strength in turn decreased the crack resistance of the heat-exposed materials.

#### *4.6. Multistage Fatigue Model Correlations*

Figure 15 shows the overall prediction of the MSF model for the 6061 and 7075 aluminum alloys, with the heat degradation accounted for through the use of material properties, microstructure information, and the constant  $\alpha$  from the incubation equation (8). The trends observed in the experimental results are satisfactorily captured by the MSF model with the relative weight of crack growth addressed. In the LCF regime, there is no appreciable degradation from the heat exposure, as mentioned earlier due to the increased ductility that compensated for the decrease in strength. In the HCF regime, however, the decreased ultimate and yield stresses in the annealed specimens became more dominant, and so a significant gap in fatigue performance is illustrated in both the experimental and modeling results.

The comparison of the results of the MSF modeling to the experimental results showed a good correlation to the 6061 aluminum alloys. In fact, the MSF model captured the trend of the 6061-A exhibiting better fatigue performance than the T6 in the LCF regime. Likewise, the model captured the experimental trend of the 6061-A exhibiting a degradation in the HCF regime. Similar to the 6061 aluminum alloy, the MSF model showed good comparison to the 7075 aluminum alloy by capturing the degradation effect due to the heat exposure. The MSF

model parameters given in Table 4 are found suitable for the peak-aged and heat effected materials.

The MSF model provides additional capability to discretize the total fatigue life into components to further correlate the proportion of the life spent incubating the crack versus that spent in the small crack growth phase, as shown in Figure 16. As expected in wrought materials, in the LCF regime, small crack growth is more influential in all four materials, but the percentage of the total life by crack incubation increases as the strain amplitude decreases until crack incubation dominates the fatigue life in the HCF regime. For the 6061 aluminum alloys, the contribution of small crack growth is a smaller percentage in the heat exposed material compared to the T6 temper over the entire range of strain amplitudes tested. However, in 7075 aluminum alloy, the opposite was observed where the small crack contribution increased significantly in the annealed compared to the T651. This is due to the difference in the ultimate strength between the two aluminum alloys, resulting in more plasticity in the 6061 aluminum alloy compared to the much lower observed plasticity in the 7075 aluminum alloy. The incubation life is a lesser component at all strain levels of both the heat-degraded materials than the peak aged materials for any given strain amplitude due to the relatively rapid increase in crack growth rate with crack length present in the heat degraded materials. Additionally, the resulting fit of the MSF model self-verifies the assumption that the long crack growth life can be neglected.

## 5. Summary

Strain-controlled fatigue tests were conducted on 6061-T6 and 7075-T651 as well as both materials after being thermally exposed for 1 hour at 1000°F. The following conclusions are reached:

1. Monotonic and strain-life fatigue tests were conducted, and the results were used to characterize the material behavior under both monotonic and cyclic loading for 6061-T6, 6061-A, 7075-T651, and 7075-A.
2. Scanning electron microscope images were used to determine preferential crack initiation sites at Fe-rich particles for the 6061 aluminum alloy and at Fe-rich particle clusters in the 7075 aluminum alloy. Crack growth rates with respect to overall crack length were also explored, and showed an increase in growth rate with crack length. Chemical (EDS) analysis was performed on the particles that initiated fatigue cracks, and these results showed that the particles are Fe-rich, similar to those found in literature [7-9].
3. Through the use of optical microscopy, statistics of particle size and nearest neighbor distance were determined. The Fe-rich particles that were found to initiate cracks were larger, on average, than the statistical particle size in the untested state.
4. By using microstructure results and mechanical properties, an MSF model was correlated to the fatigue behavior of both the peak-aged and heat-degraded aluminum alloys. These different heat-treatments were captured using one unique set of model constants, with

only the material constants and the small crack growth exponent updated for a given material.

## References

1. ASM International Handbook Committee, ASM Specialty Handbook: Aluminum and Aluminum Alloys. Davis J.R., Ed., Materials Park: ASM International 1993.
2. Dorward R.C., and Bouvier C., A rationalization of factors affecting strength, ductility, and toughness of AA6061-type Al-Si-Mg-(Cu) alloys. *Mater. Sci. and Eng* 1998; A254: 33-44.
3. Prietto M., Tsang M., Hernandez S. The effects of heat damage of aluminum 6061-T6 AM-2 mats and high-power run-up anchor. *Engineering Failure Analysis* 2011; 18:124-137.
4. Mrówka-Nowotnik G. Influence of chemical composition variation and heat treatment on microstructure and mechanical properties of 6XXX alloys. *Archives of Material Science and Engineering* 2010; 46:2:98-107.
5. Tajally M, Emadoddin E. Mechanical and anisotropic behaviors of 7075 aluminum alloy sheets. *Materials and Design* 2011; 32:1594-1599.
6. McDowell D.L., Gall K., Horstemeyer M.F., and Fan J. Microstructure-Based Fatigue Modeling of Cast A356-T6 Alloy. *Engineering Fracture Mechanics* 2003; 70:49-80.
7. Xue Y., McDowell D.L., Horstemeyer M.L., Dale M.H., and Jordon J.B.. Microstructure-based Multistage Fatigue Modeling of Aluminum Alloy 7075-T651. *Engineering Fracture Mechanics* 2007; 74:17:2810-2823.
8. Xue, Y., El Kadiri, H., Horstemeyer, M.F., Jordon, J.B., Weiland, H., Micromechanisms of Multistage Crack Growth in a High-Strength Aluminum Alloy, *Acta Materialia* 2007; 55(6):1975-1984.
9. Xue, Y., McDowell, D.L., Horstemeyer, M.F., Dale, M., Jordon, J.B., Microstructure-based multistage fatigue modeling of aluminum alloy 7075-T651. *Engineering Fracture Mechanics* 2007; 74:2810-2823.
10. Xue, Y, Horstemeyer, M.F McDowell, D, El Kadiri, H., and Fan, J., Microstructure-based multistage fatigue modeling of a cast AE44 magnesium alloy. *Int J. Fatigue* 2007; 29:666–676.

11. Xue, Y., Pascu, A., Horstemeyer, M.F., Wang, L., Wang, P.T., Microporosity effects on cyclic plasticity and fatigue of LENS(TM)-processed steel, *Acta Materialia* 2010;58(11):4029-4038.
12. Jordon, J.B., Horstemeyer, M.F., Bernard, J.D., Solanki, K., Berry, J.T. Damage Characterization and Modeling of a 7075-T651 Aluminum Plate. *Mat Sci Eng. A* 2009; 527, 1-2:169-178.
13. Jordon, J.B., Horstemeyer, M.F., Yang, N. Major, J.F. Gall, K. Fan, J. McDowell, D.L. Microstructural Inclusion Influence on Fatigue of a Cast A356 Aluminum Alloy, *Metallurgical and Materials Trans A* 2010; 41(2):356-363.
14. Jordon J.B., Horstemeyer M.F., Yang N., Major J.F., Gall K., Fan J., McDowell D.L. Microstructural Inclusion Influence on Fatigue of a Cast A356 Aluminum Alloy. *Metallurgical and Materials Trans A* 2009; 41: 356-363.
15. Lugo M., Jordon J.B., Solanki K.N., Hector Jr. L.G., Bernard J.D., Luo A.A., Horstemeyer, M.F., Role of Different Material Processing Methods on the Fatigue Behavior of AZ31 Magnesium Alloy. *International Journal of Fatigue* 2013 (Accepted).
16. Jordon, J.B., Horstemeyer, M.F., Solanki, K., Xue, Y., 2007. Damage and stress state influence on the Bauschinger effect in aluminum alloys. *Mechanics of Materials*, 39:920-931.
17. Annual Book of ASTM Standards. Metals test methods and analytical procedures. vol. 03.01. West Conshohocken, PA: ASTM; 2003.
18. Basquin O.H., The Exponential Law of Endurance Tests. *Am. Soc. Testing Mater. Proc.* 1910; 10: 625–630.
19. Dieter G.E.. *Mechanical Metallurgy*, Third Edition, McGraw-Hill 1986.
20. Bannantine J.A., Comer J.J., Handrock J.L., *Fundamentals of Metal Fatigue*. New Jersey: Prentice Hall, 1997.
21. Stephens R.I., Fatemi A., Stephens R.R., Fuchs H.O., *Metal Fatigue in Engineering*. 2nd ed. New York: John Wiley & Sons, 2001.
22. Jordon J.B., Gibson, J.B., Horstemeyer, M.F., Kadiri H.E., Baird, J.C., Luo A.A., Effect of Twinning, Slip, and Inclusions on the fatigue anisotropy of extrusion-textured AZ61 magnesium alloy. *Material Science and Engineering A* 2011; 528(22): 6860-6871.
23. Gall K., Horstemeyer M.F., McDowell D.L., and Fan J. Finite Element Analysis of the stress distributions Near Damaged Si Particles Clusters in Case Al-Si Alloys. *Mechanics of Materials* 2000; 32:277-301.

24. Hayhurst D.R., Leckie D.L., McDowell, D.L. Damage growth under non-proportional loading. ASTM STP 1985; 853: 553-558.
25. Agarwal H., Gokhale A.M., Graham S., Horstemeyer M.F. Void growth in 6061-aluminum alloy under triaxial stress state, Material Science and Engineering 2003; A341:35-42.

**Table 1.** Monotonic Properties of 6061-T6, 6061-A, 7075-T651, and 7075-A.

<b>Property</b>	<b>Extruded 6061-T6</b>	<b>Extruded 6061 - A</b>	<b>Extruded 7075-T651</b>	<b>Extruded 7075-A</b>
Young's Modulus	67.8 GPa	66.7 GPa	71.6 GPa	70.7 GPa
0.2% Yield Strength	233 MPa	93.4MPa	538.6 MPa	209 MPa
Monotonic Stress-Strain Coefficient (K)	178 MPa	337.58 MPa	631.5 MPa	756.7 MPa
Strain Hardening Exp. (n)	0.360	0.2234	0.0345	0.2326
U T S	320 MPa	223.5 MPa	665.8 MPa	497.7 MPa

**Table 2.** List of tested specimens, including cycles to failure and strain amplitude ( \* indicates runout).

<b>Specimen</b>	<b>Material</b>	<b>Strain Amplitude (mm/mm)</b>	<b>Cycles to Failure</b>	<b>Diameter (mm)</b>
T-6-1	6061-T6	0.006	1326	6.29
T-6-2	6061-T6	0.005	2181	6.30
T-6-3	6061-T6	0.004	4551	6.32
T-6-4	6061-T6	0.003	25378	6.33
T-6-5	6061-T6	0.002	1873032*	6.31
T-6-6	6061-T6	0.006	720	6.30
T-6-7	6061-T6	0.006	995	6.22
T-6-8	6061-T6	0.003	42761	6.27
T-6-9	6061-T6	0.004	3750	6.28
T-6-10	6061-T6	0.005	1597	6.22
T-6-11	6061-T6	0.003	14538	6.32
T-6-12	6061-T6	0.003	22479	6.27
T-6-13	6061-T6	0.004	6535	6.29
T-6-14	6061-T6	0.005	2047	6.29
T-6-15	6061-T6	0.007	721	6.32
T-6-16	6061-T6	0.005	4622	6.35
T-6-17	6061-T6	0.005	2138	6.32
T-6-18	6061-T6	0.006	1024	6.36
T-6-19	6061-T6	0.004	5537	6.35
T-6-20	6061-T6	0.004	6699	6.39
T-6-21	6061-T6	TENSION	TENSION	6.39
			(0.001mm/mm/s)	
T-6-22	6061-T6	0.006	1354	6.30
T-6-23	6061-T6	0.007	850	6.34
T-6-24	6061-T6	0.005	1241	6.36
T-6-25	6061-T6	0.003	70036	6.35
A-6-1	6061-A	TENSION	TENSION	6.32
			(0.001mm/mm/s)	
A-6-2	6061-A	0.007	1426	6.38
A-6-3	6061-A	0.005	1171	6.34
A-6-4	6061-A	0.006	1246	6.34
A-6-5	6061-A	0.006	2764	6.38
A-6-6	6061-A	0.005	893	6.34
A-6-7	6061-A	0.005	794	6.32
A-6-8	6061-A	0.007	1634	6.35
A-6-9	6061-A	0.003	13034	6.34
A-6-10	6061-A	0.004	5657	6.32
A-6-11	6061-A	0.004	6661	6.32
A-6-12	6061-A	0.003	11594	6.34
T-7-1	7075-T651	0.006	1024	6.36

---

<b>T-7-2</b>	7075-T651	0.004	22410	6.40
<b>T-7-3</b>	7075-T651	0.004	75142	6.38
<b>T-7-4</b>	7075-T651	0.006	8863	6.38
<b>T-7-5</b>	7075-T651	0.006	5890	6.35
<b>T-7-6</b>	7075-T651	0.005	7876	6.30
<b>T-7-7</b>	7075-T651	0.007	1252	6.29
<b>T-7-8</b>	7075-T651	0.007	2806	6.34
<b>T-7-9</b>	7075-T651	0.006	62360	6.31
<b>T-7-10</b>	7075-T651	0.005	15868	6.32
<b>T-7-11</b>	7075-T651	0.005	12260	6.30
<b>T-7-12</b>	7075-T651	0.006	3197	6.37
<b>T-7-13</b>	7075-T651	0.007	2411	6.32
<b>T-7-14</b>	7075-T651	0.0045	52825	6.34
<b>T-7-15</b>	7075-T651	0.004	96045	6.32
<b>T-7-16</b>	7075-T651	0.004	71234	6.33
<b>T-7-17</b>	7075-T651	0.004	165165	6.35
<b>T-7-18</b>	7075-T651	0.004	116568	6.33
<b>T-7-19</b>	7075-T651	0.0045	32642	6.35
<b>T-7-20</b>	7075-T651	0.0045	47341	6.33
<b>T-7-21</b>	7075-T651	0.003	2545805*	6.36
<b>T-7-22</b>	7075-T651	TENSION	TENSION	6.34
			(0.001mm/mm/s)	
<b>T-7-23</b>	7075-T651	0.008	724	6.40
<b>T-7-24</b>	7075-T651	0.009	515	6.40
<b>A-7-1</b>	7075-A	0.007	1617	6.34
<b>A-7-2</b>	7075-A	0.006	2359	6.33
<b>A-7-3</b>	7075-A	0.005	5406	6.36
<b>A-7-4</b>	7075-A	0.004	10024	6.35
<b>A-7-5</b>	7075-A	0.003	49965	6.35
<b>A-7-6</b>	7075-A	0.007	1107	6.33
<b>A-7-7</b>	7075-A	0.006	1495	6.34
<b>A-7-8</b>	7075-A	0.005	6117	6.32
<b>A-7-9</b>	7075-A	0.004	21467	6.38
<b>A-7-10</b>	7075-A	0.003	61437	6.32
<b>A-7-11</b>	7075-A	TENSION	TENSION	6.33
			(0.001mm/mm/s)	

---

**Table 3.** Cyclic Properties of 6061-T6, 6061-A, 7075-T652, and 7075-A.

<b>Property</b>	<b>Extruded 6061-T6</b>	<b>Extruded 6061-A</b>	<b>Extruded 7075-T651</b>	<b>Extruded 7075-A</b>
Cyclic Yield Stress	270 MPa	180 MPa	532 MPa	274 MPa
Cyclic Stress Strain Coefficient (K')	502.8 MPa	238.6 MPa	792.8 MPa	457.5 MPa
Cyclic Strain Hardening Exponent (n')	0.0737	0.0353	0.0662	0.0826
Fatigue strength coefficient, ( $\sigma_f$ )	705 MPa	240.12 MPa	952.3 MPa	601.1 MPa
Fatigue Strength exponent (b)	-0.11	-0.029	-0.089	-0.091
Fatigue ductility coefficient ( $\epsilon_f$ )	2.40	2.24	0.182	25.7
Fatigue ductility exponent (c)	-0.98	-0.86	-0.43	-1.1

**Table 4.** Multistage Fatigue (MSF) Model constants.

	Constant	6061-	6061-	7075-	7075-	Description
		T6	A	T651	A	
Crack Incubation	$C_m$	0.3	0.3	0.3	0.3	Coefficient in Modified Coffin Manson Law (Eq. 8)
	$\alpha$	-0.95	-0.65	-1.50	-0.90	Ductility exponent in Modified Coffin Manson Law (Eq. 8)
	$q$	4.7	4.7	4.7	4.7	Exponent in remote strain to local plastic shear strain (Eq. 9 & 10)
	$y_I$	100	100	100	100	Constant in remote strain to local plastic shear strain (Eq. 9 & 10)
	$y_2$	500	500	500	500	Linear constant in remote strain to local plastic shear strain (Eq. 9 & 10)
	$\xi$	2	2	2	2	Geometric factor in micromechanics study (Eq. 10)
	$r$	0.3	0.3	0.3	0.3	Exponent in micromechanics study (Eq. 12)
	$\omega$	0.5	0.5	0.5	0.5	Omega (Eq. 14)
	Small Crack Growth	$\Theta$	0	0	0	0
$\zeta$		3.5	3.5	3.5	3.5	Exponent in Small crack growth (Eq. 14)
$C_I$		500000	500000	500000	500000	HCF constant in small crack growth (Eq. 14)
$C_{II}$		0.05	0.05	0.05	0.05	LCF constant in small crack growth (Eq. 14)
$\chi$		0.35	0.35	0.35	0.35	Crack growth rate constant (Eq. 13)

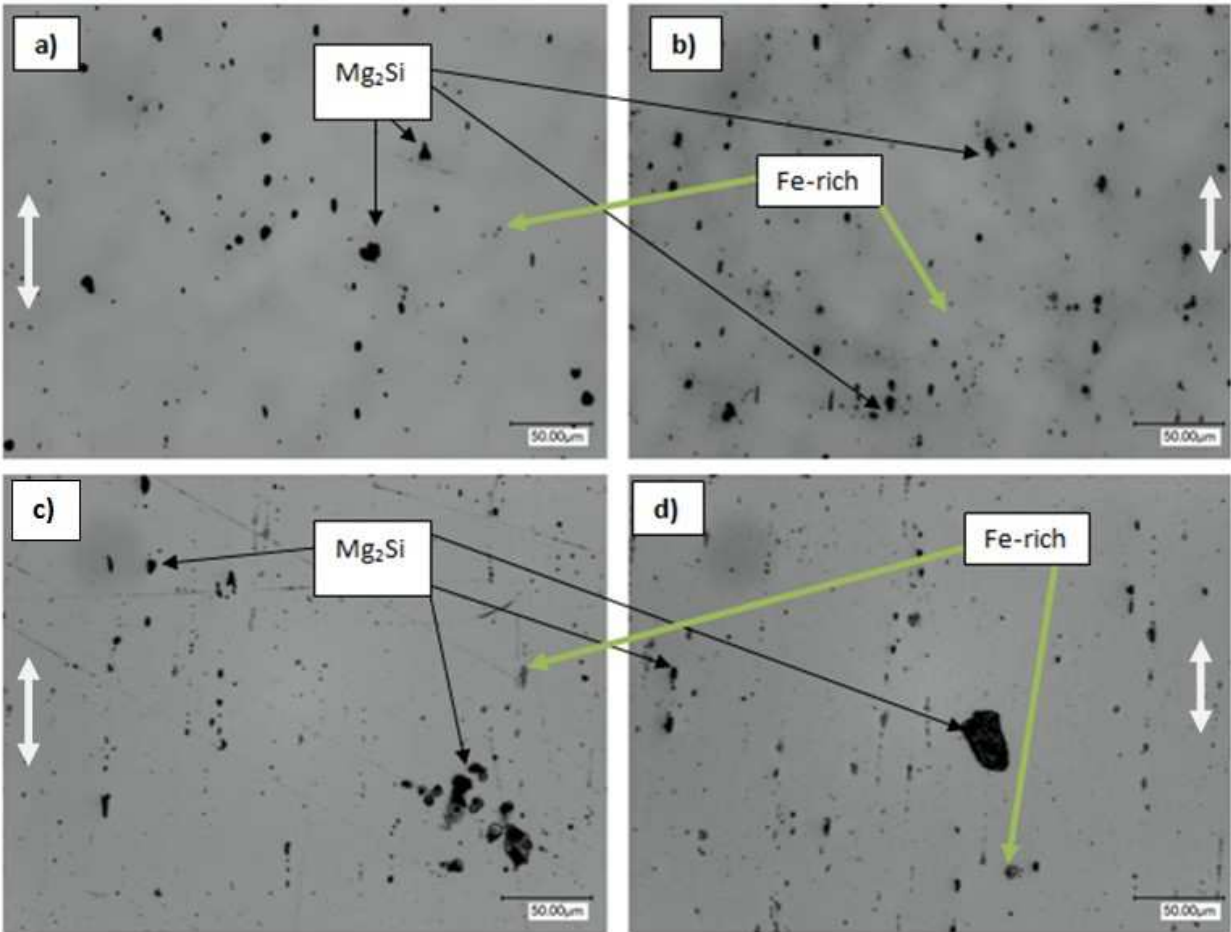


**Figure 1.** The intermetallic particles of a) 6061-T6, b) 6061-A, c) 7075-T651, and d) 7075-A aluminum alloys.

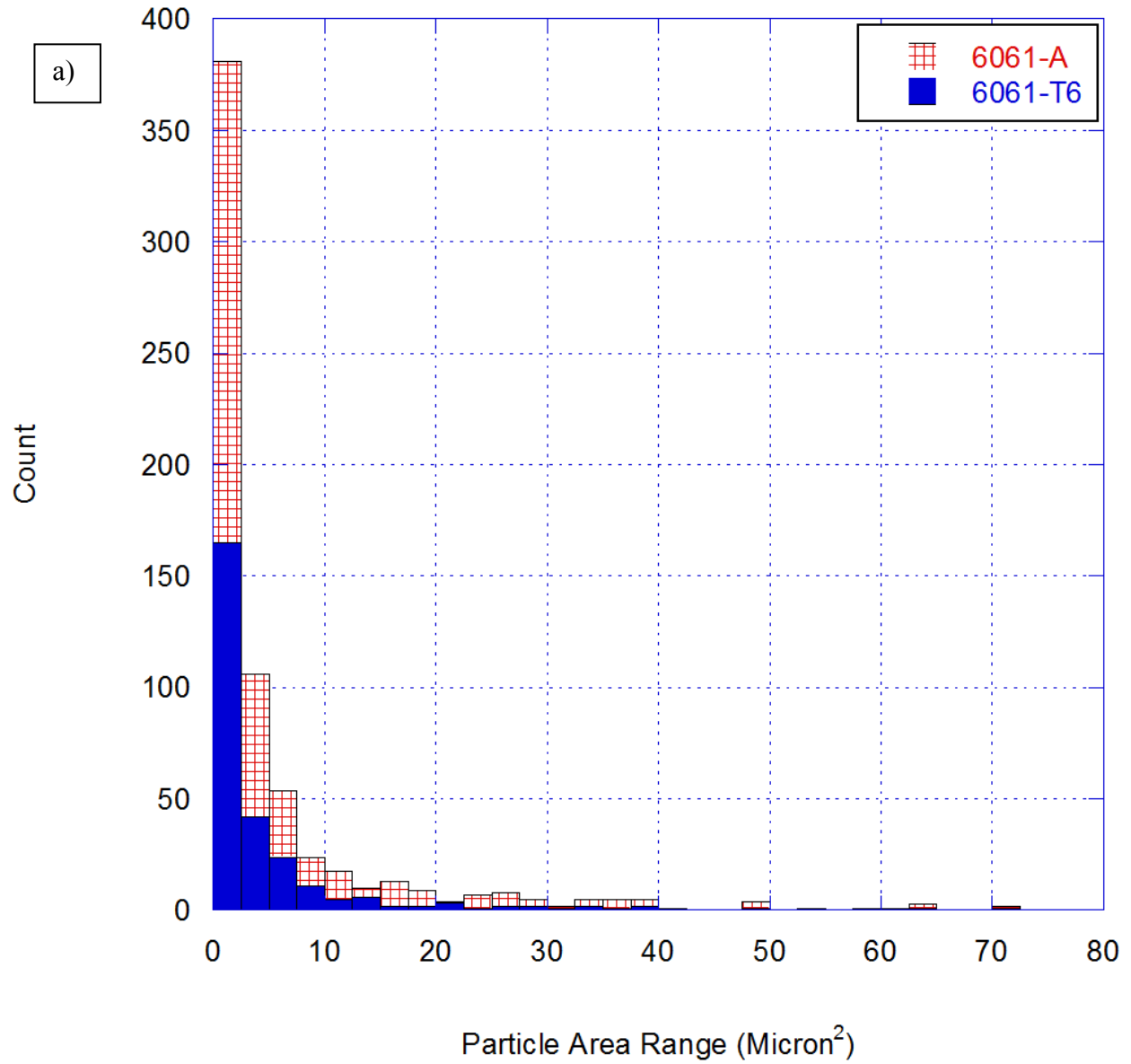


**Figure 2.** Histogram of the area of individual intermetallic particles for a) 6061 and b) 7075 aluminum alloys.

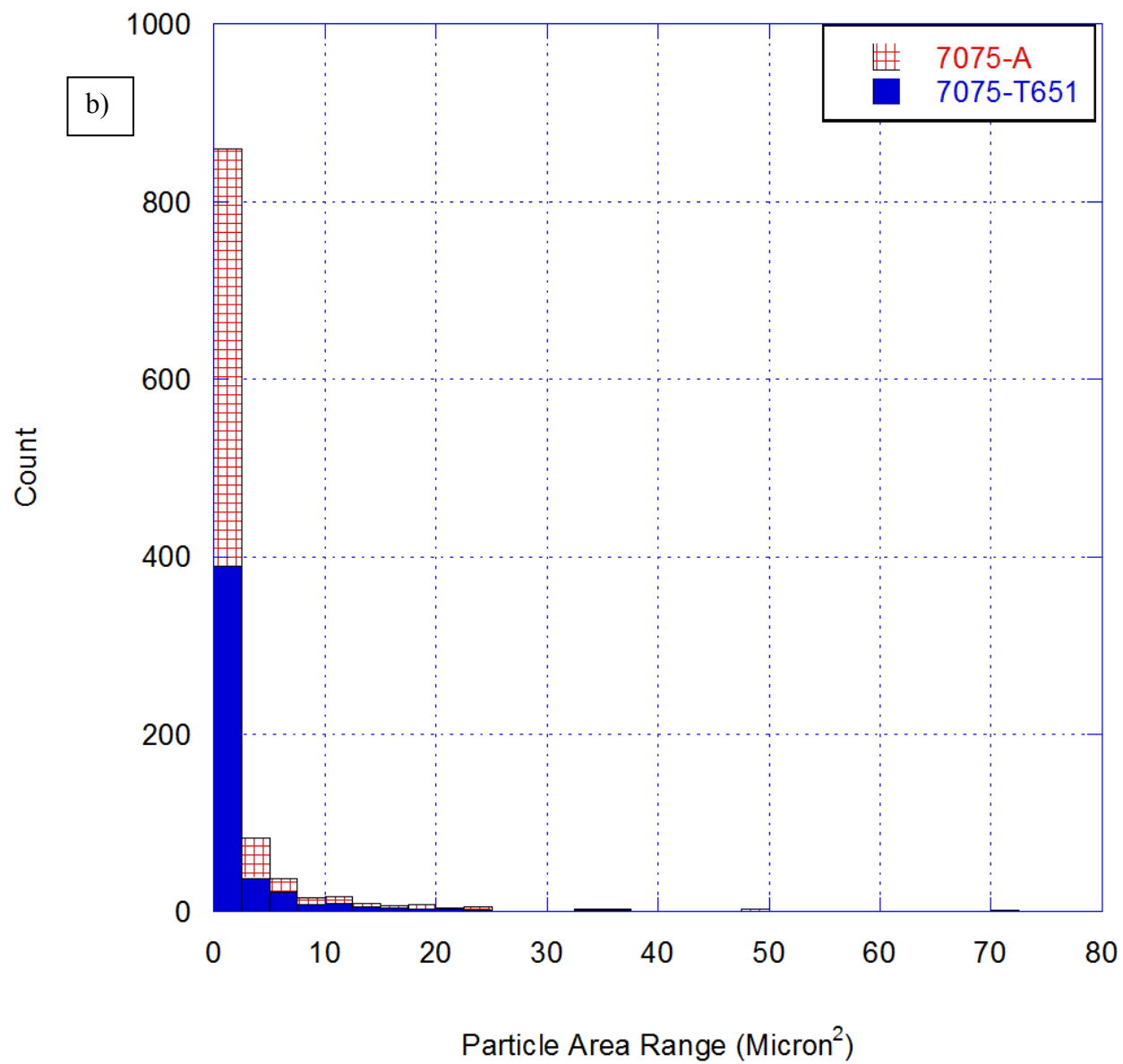


**Figure 2.** Histogram of the area of individual intermetallic particles for a) 6061 and b) 7075 aluminum alloys (continuing).

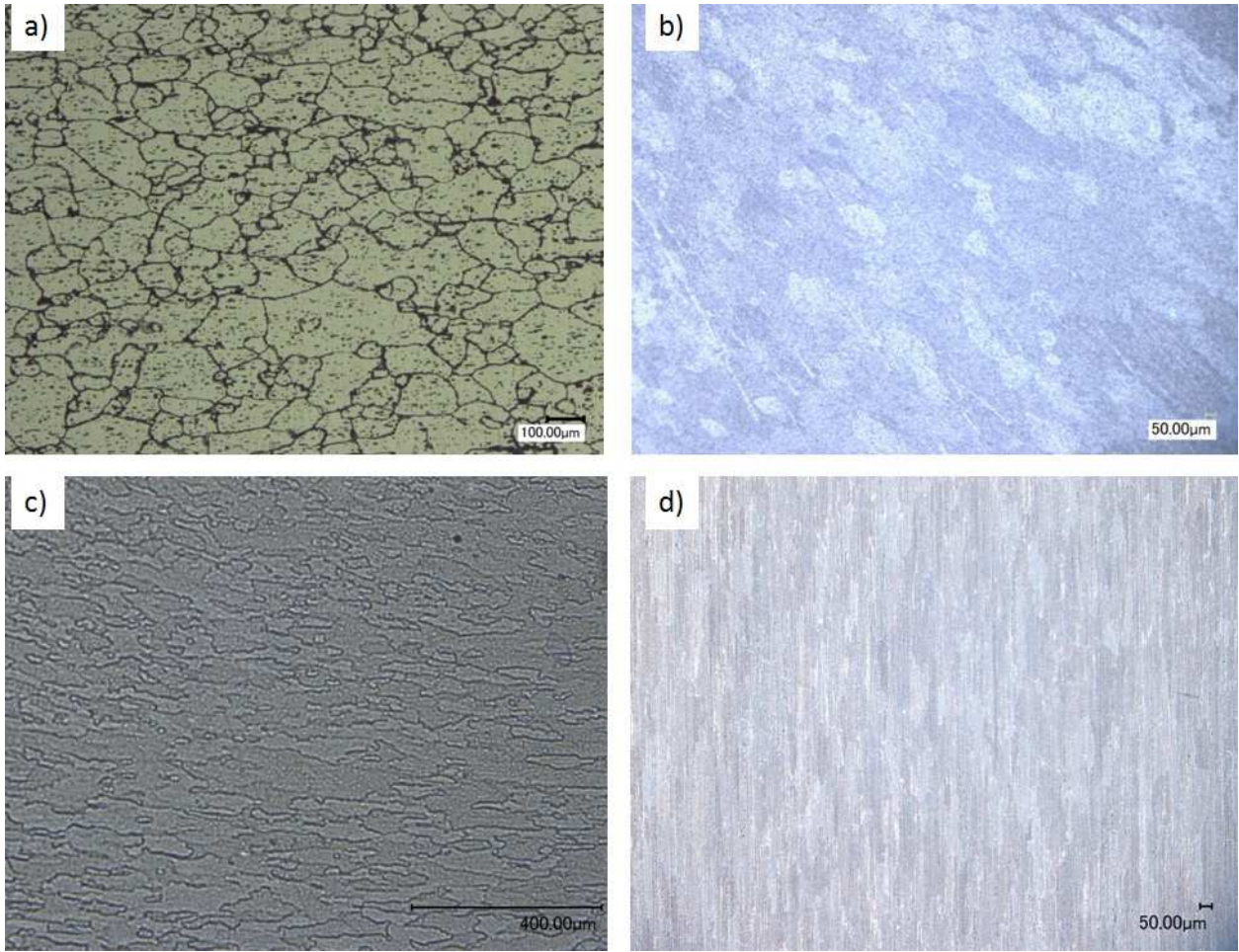


**Figure 3.** The etched microstructure of a) 6061-T6, b) 6061-A, c) 7075-T651, and d) 7075-A aluminum alloys.

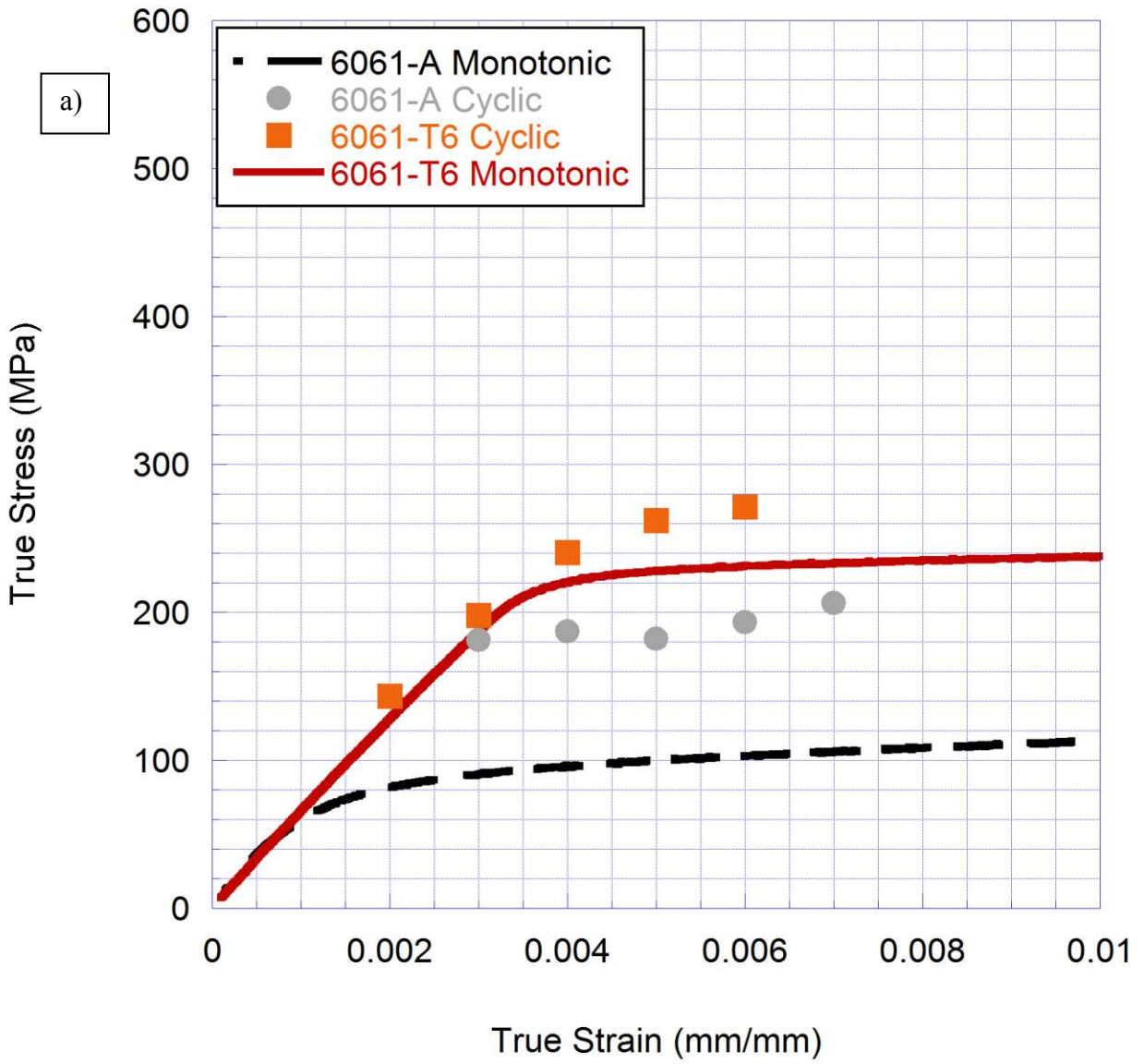


**Figure 4.** The monotonic and cyclic stress strain curves for a) 6061 and b)7075 aluminum alloys.

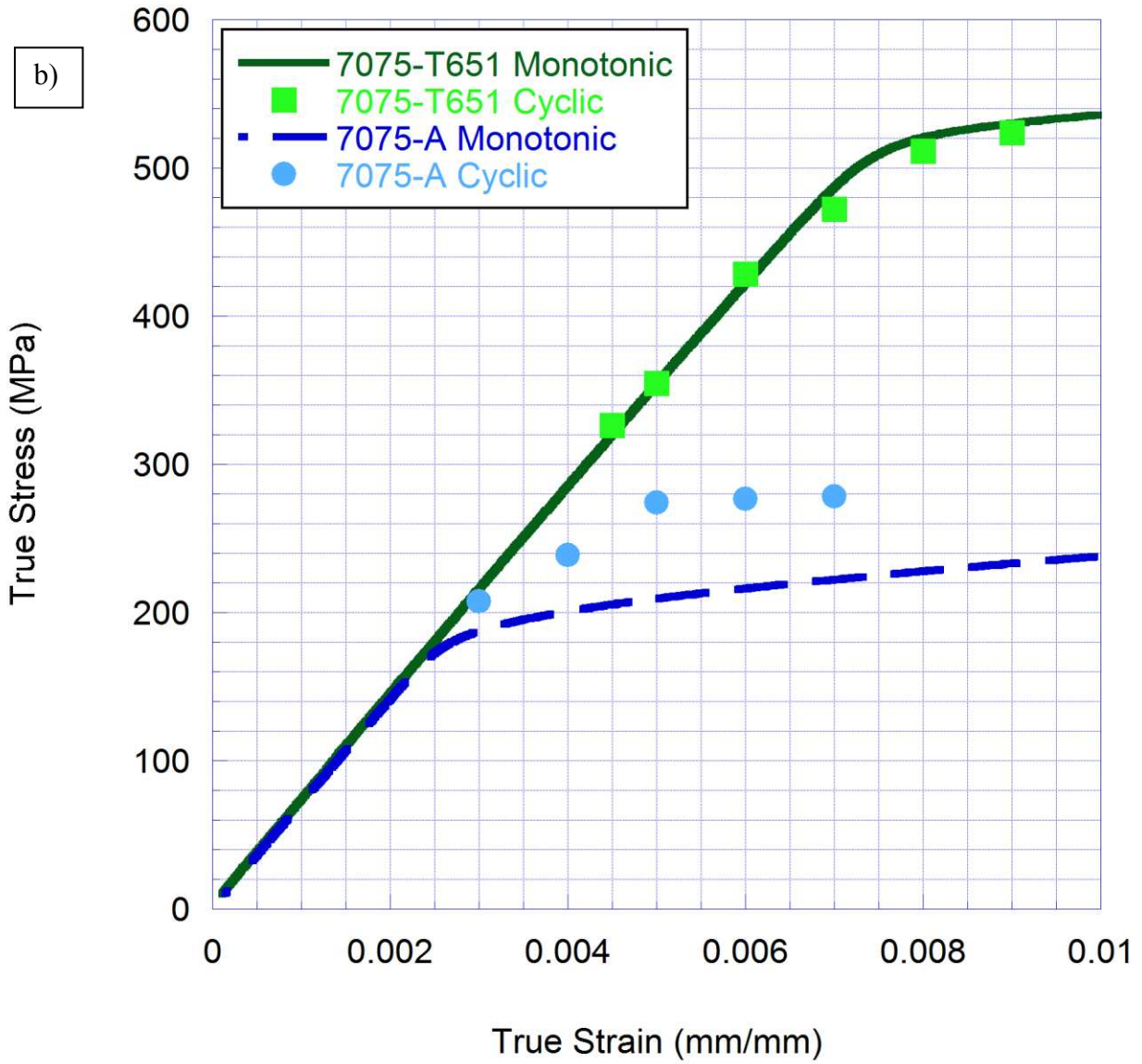


**Figure 4.** The monotonic and cyclic stress strain curves for a) 6061 and b)7075 aluminum alloys (continuing).

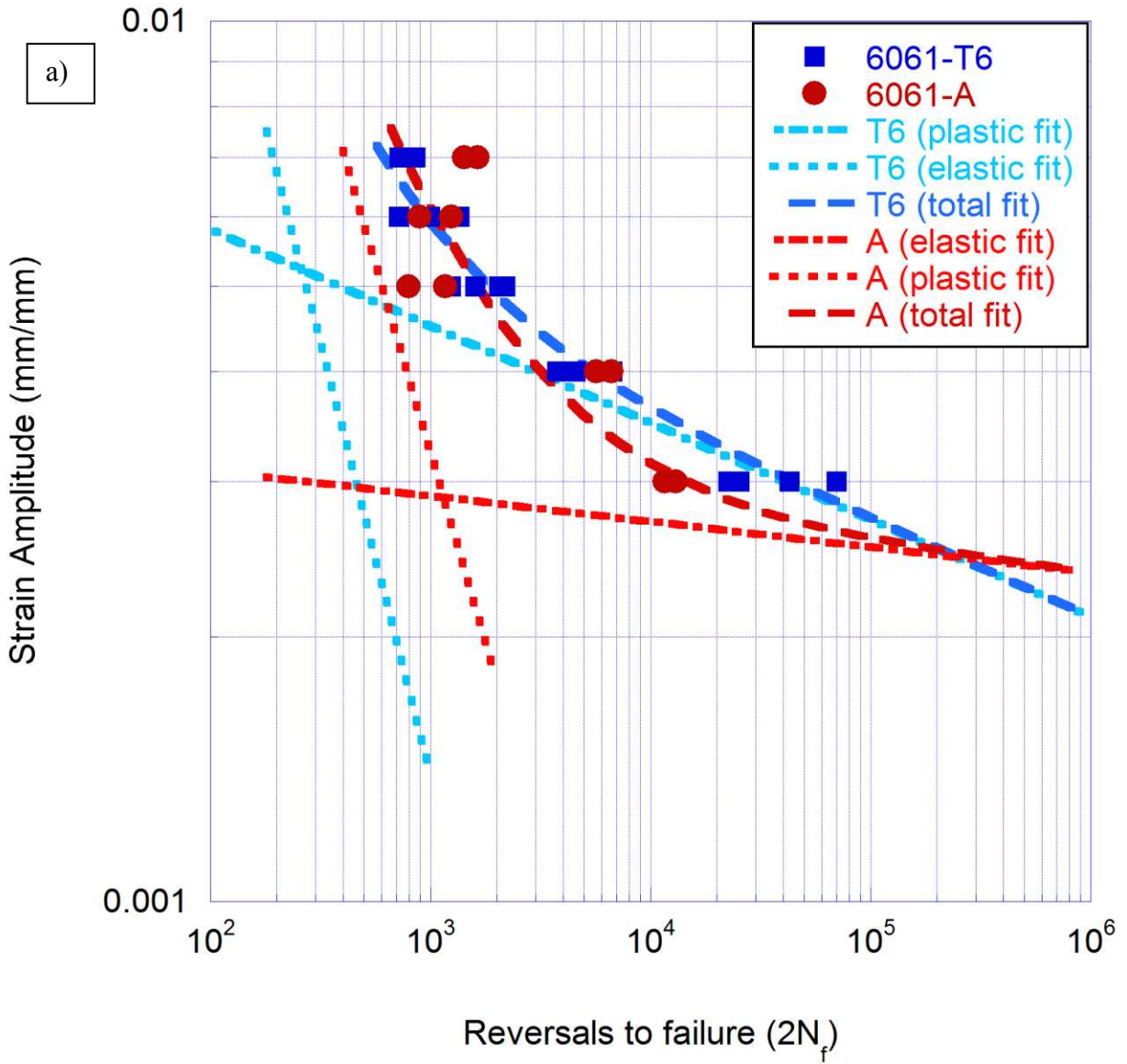


**Figure 5.** The strain-life equation fits for a) 6061 and b) 7075 aluminum alloys.

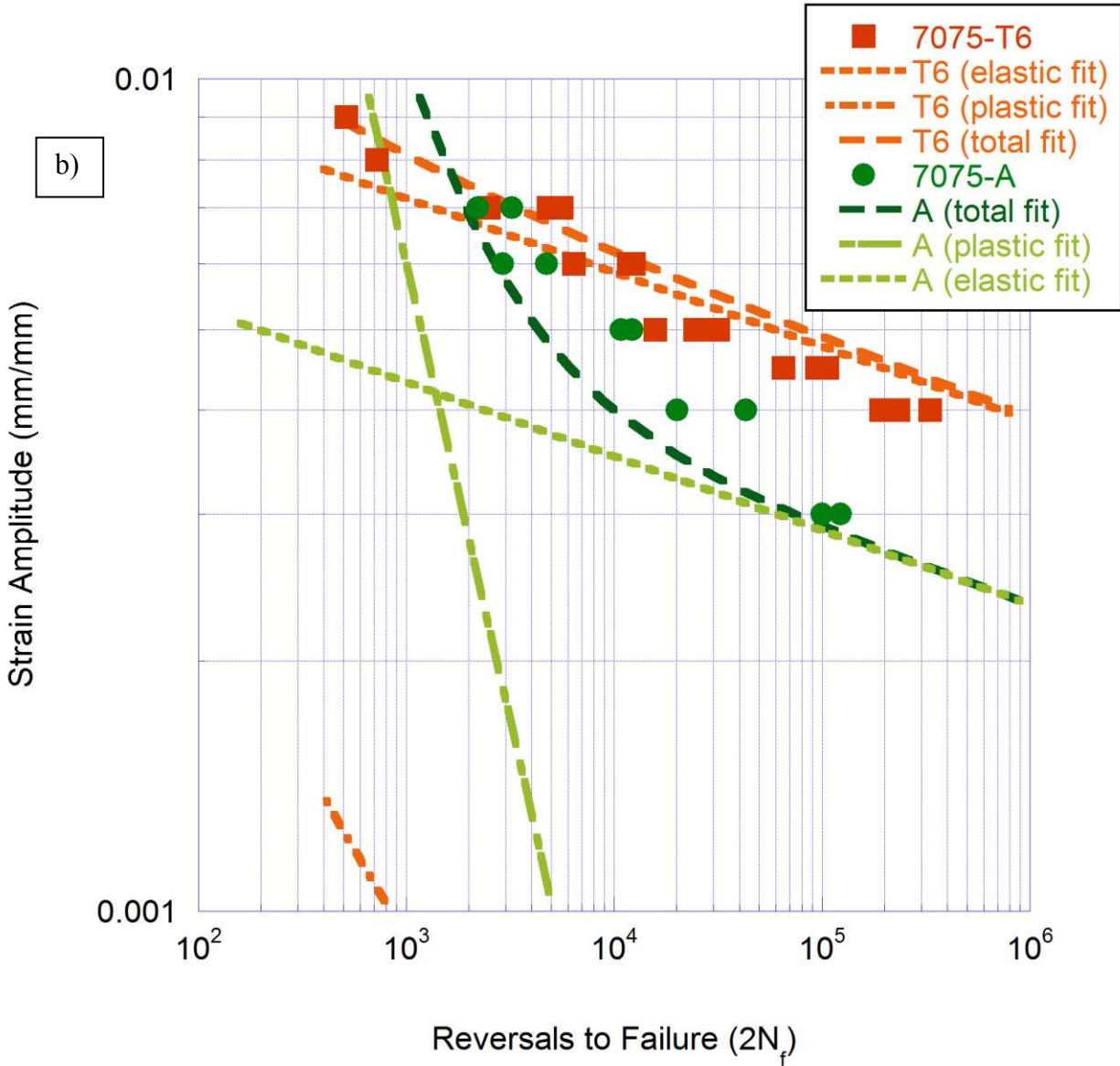


**Figure 5.** The strain-life equation fits for a) 6061 and b) 7075 aluminum alloys (continuing).

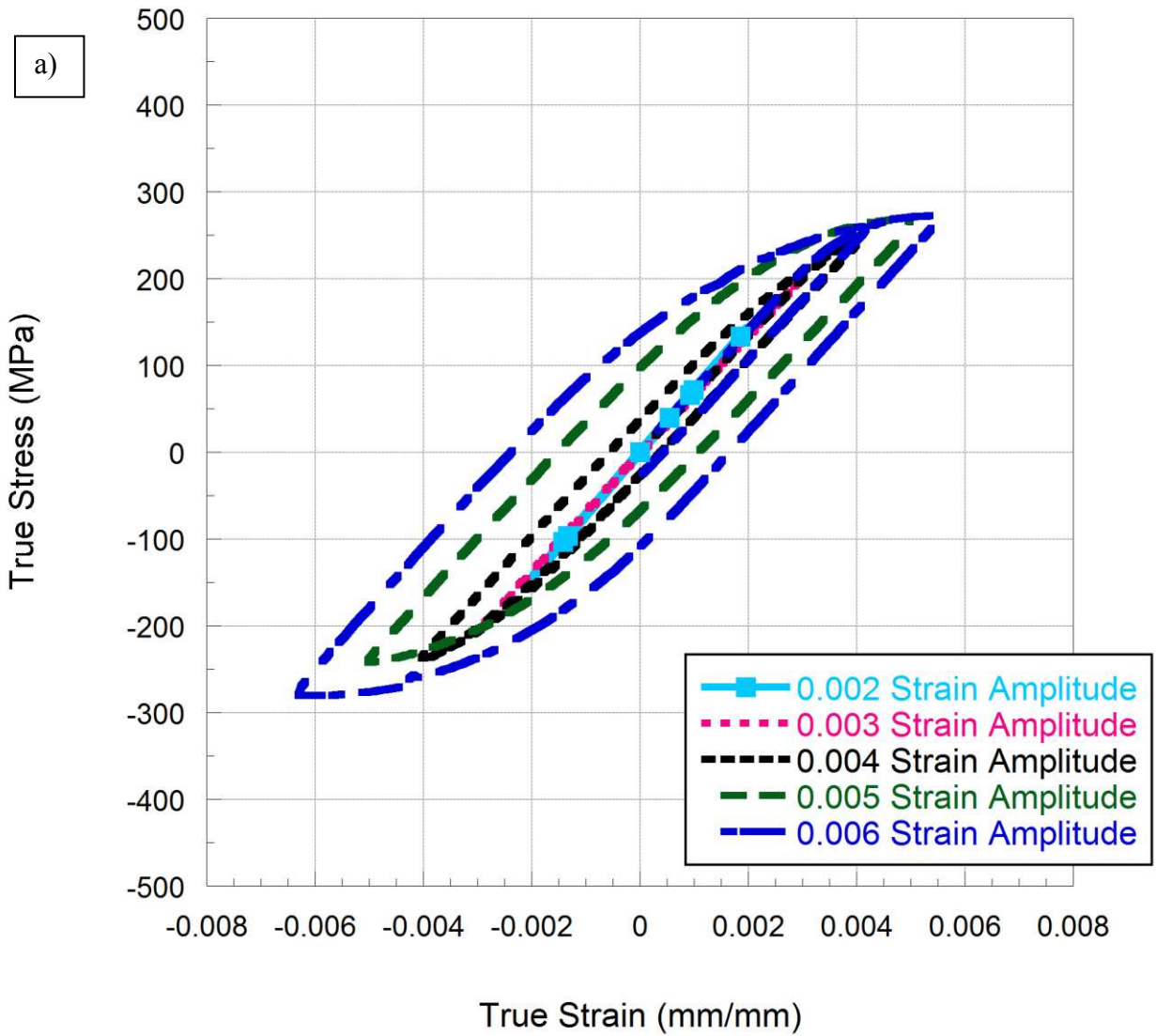


**Figure 6.** The first cycle hysteresis loops for the a) 6061-T6, b) 6061-A, c) 7075-T651, and d) 7075-A aluminum alloys.

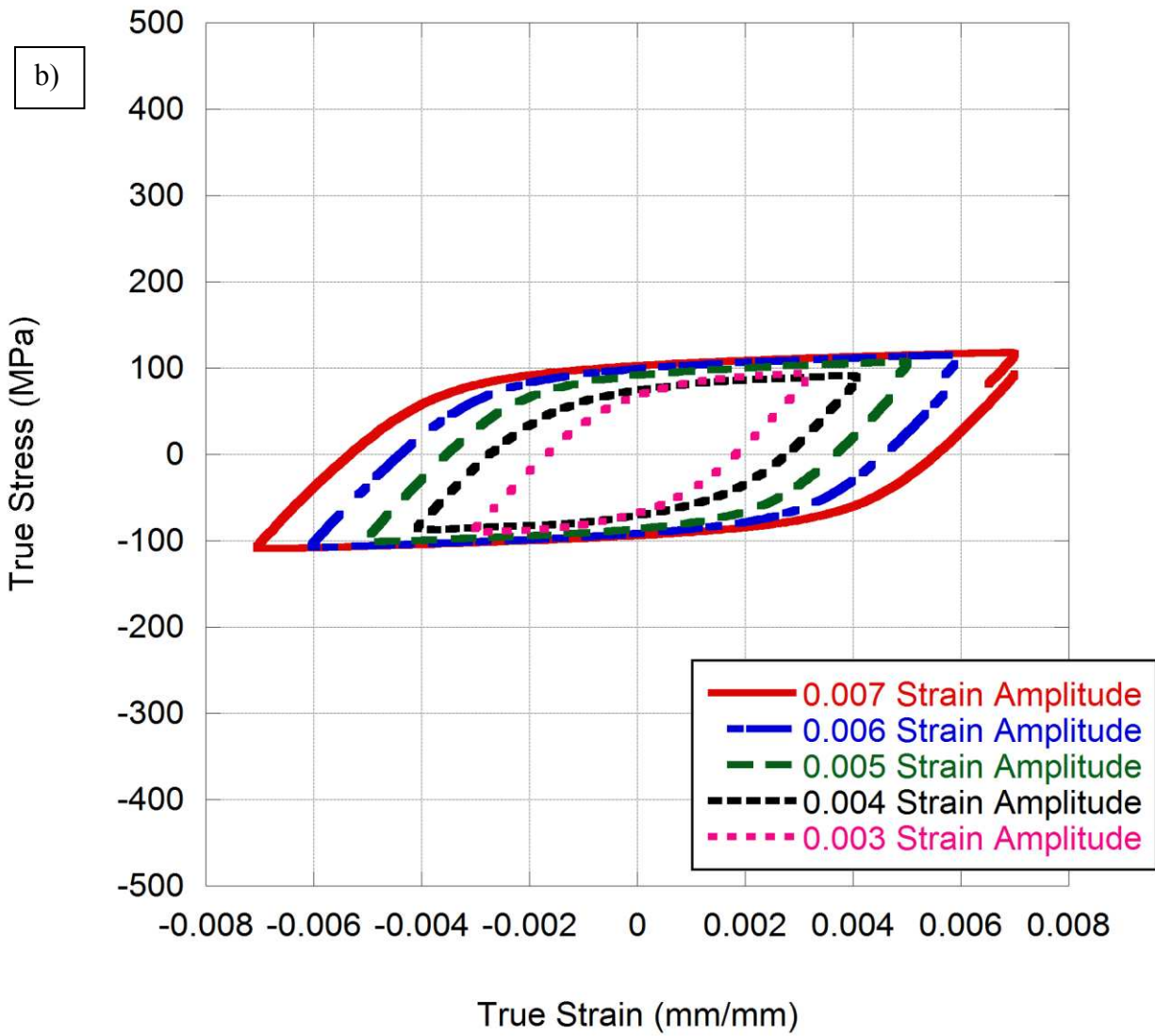


**Figure 6.** The first cycle hysteresis loops for the a) 6061-T6, b) 6061-A, c) 7075-T651, and d) 7075-A aluminum alloys (continuing).

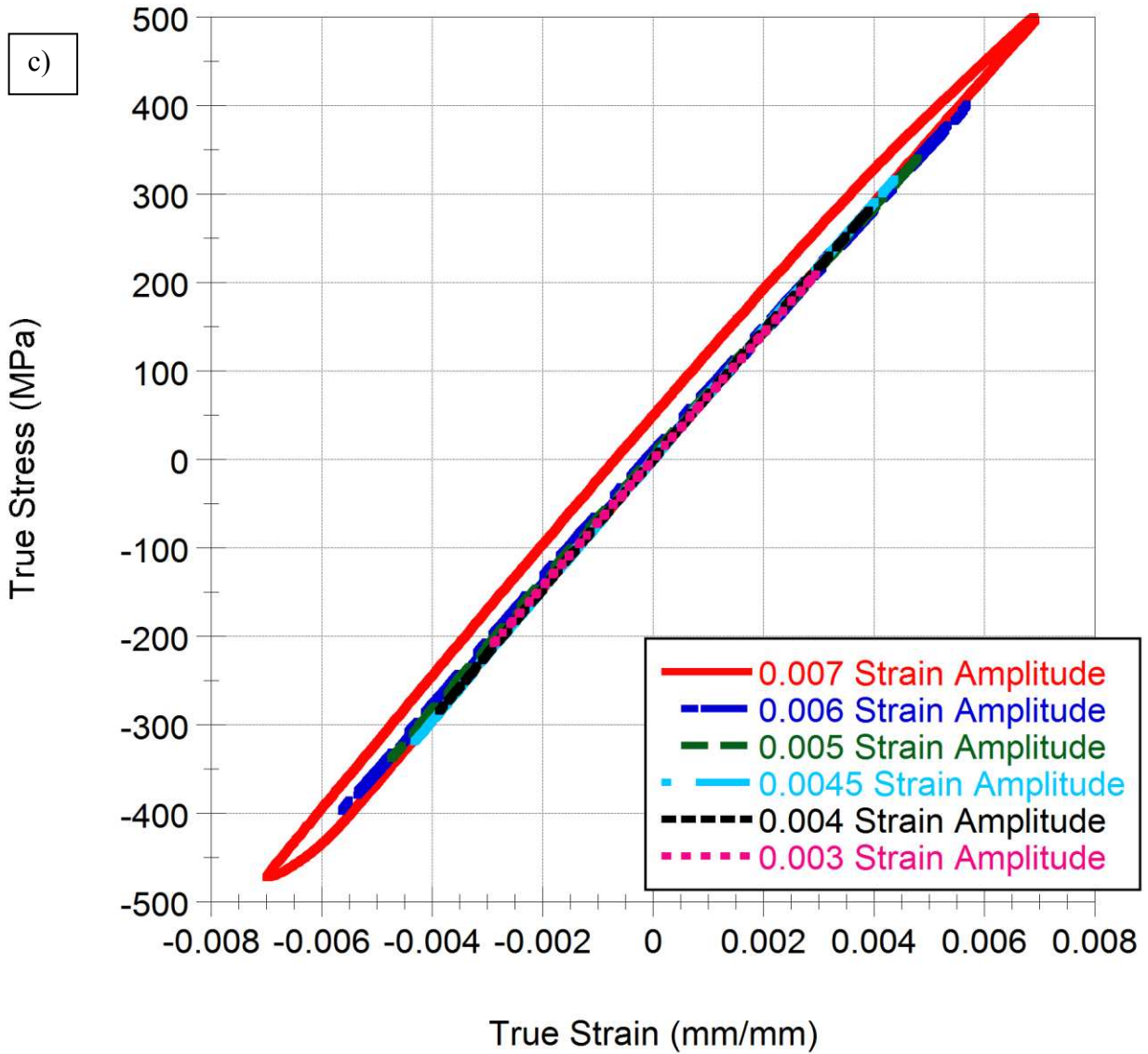


**Figure 6.** The first cycle hysteresis loops for the a) 6061-T6, b) 6061-A, c) 7075-T651, and d) 7075-A aluminum alloys (continuing).

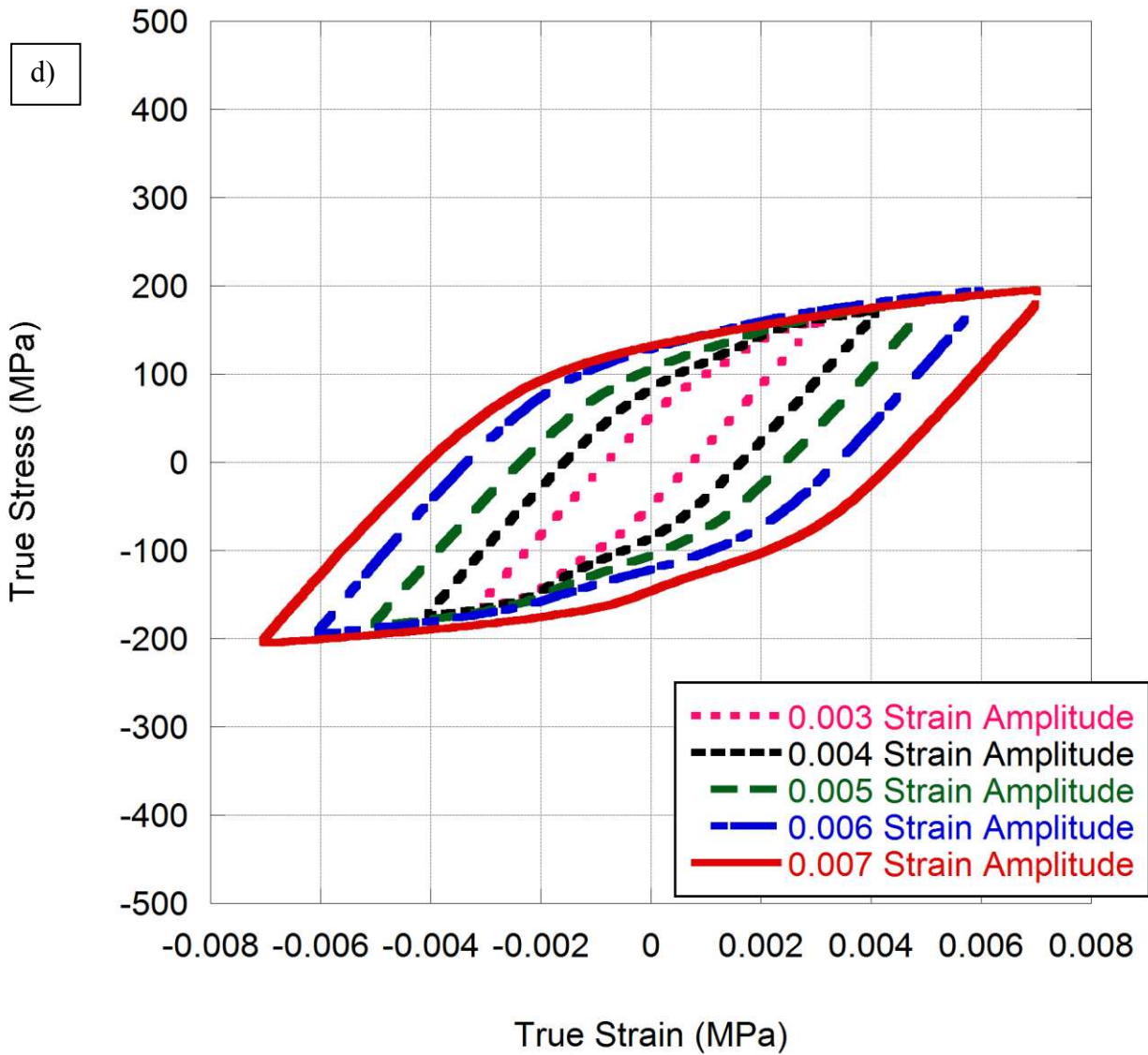


**Figure 6.** The first cycle hysteresis loops for the a) 6061-T6, b) 6061-A, c) 7075-T651, and d) 7075-A aluminum alloys (continuing).

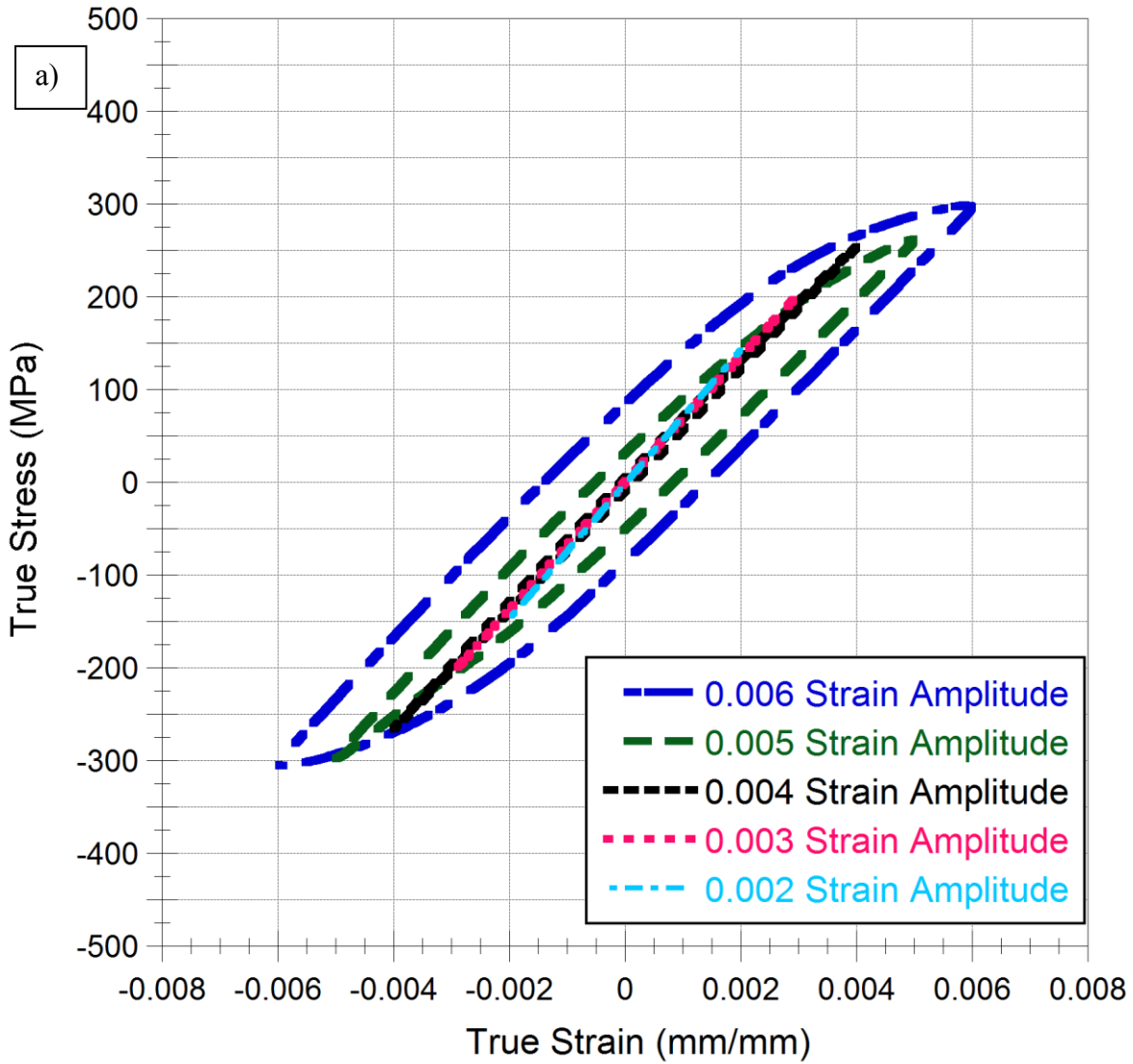


**Figure 7.** Stabilized (mid-cycle) hysteresis cycles for a) 6061-T6, b) 6061-A, c) 7075-T651, and d) 7075-A aluminum alloys.

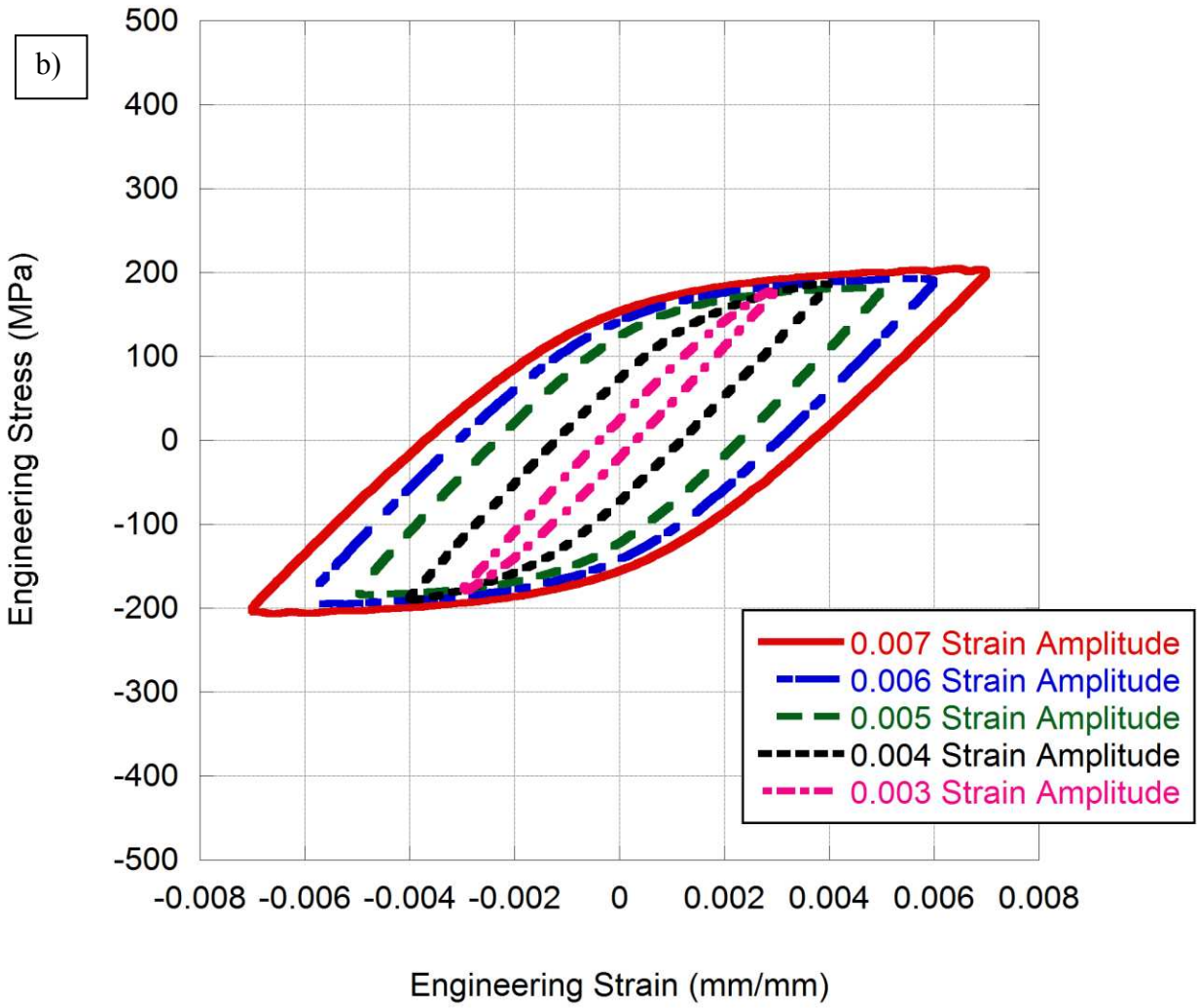


**Figure 7.** Stabilized (mid-cycle) hysteresis cycles for a) 6061-T6, b) 6061-A, c) 7075-T651, and d) 7075-A aluminum alloys (continuing).

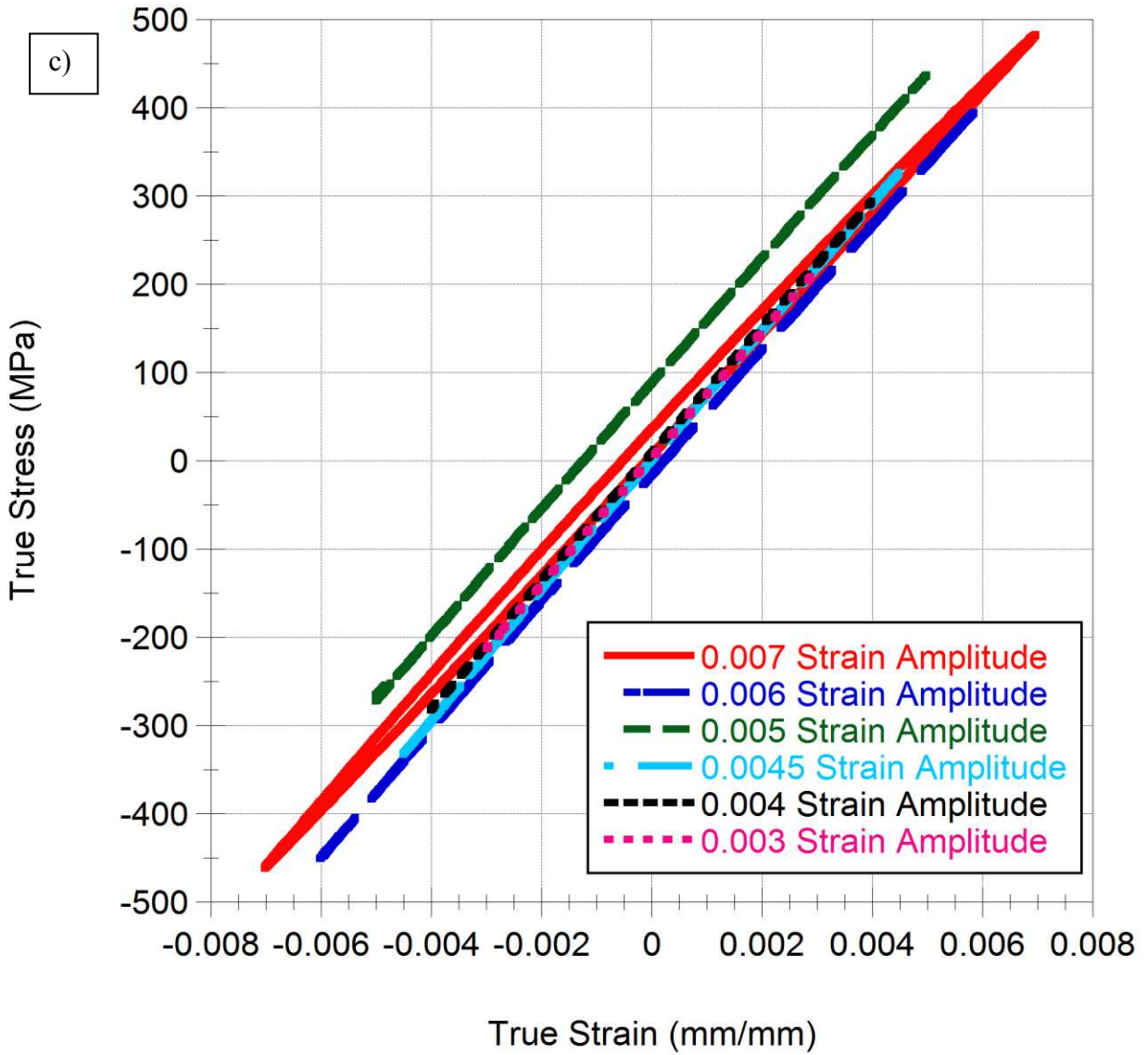


**Figure 7.** Stabilized (mid-cycle) hysteresis cycles for a) 6061-T6, b) 6061-A, c) 7075-T651, and d) 7075-A aluminum alloys (continuing).

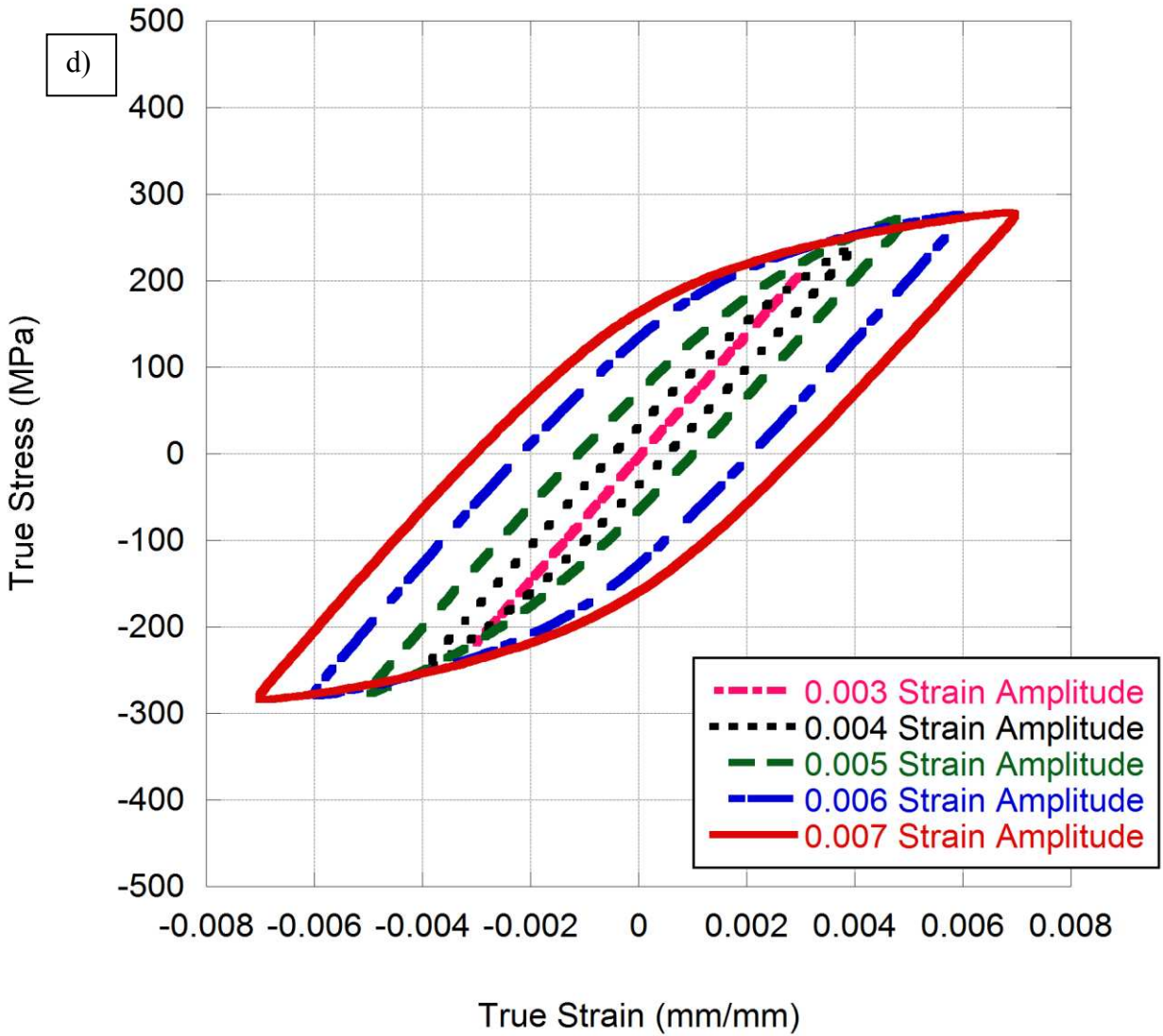


**Figure 7.** Stabilized (mid-cycle) hysteresis cycles for a) 6061-T6, b) 6061-A, c) 7075-T651, and d) 7075-A aluminum alloys (continuing).

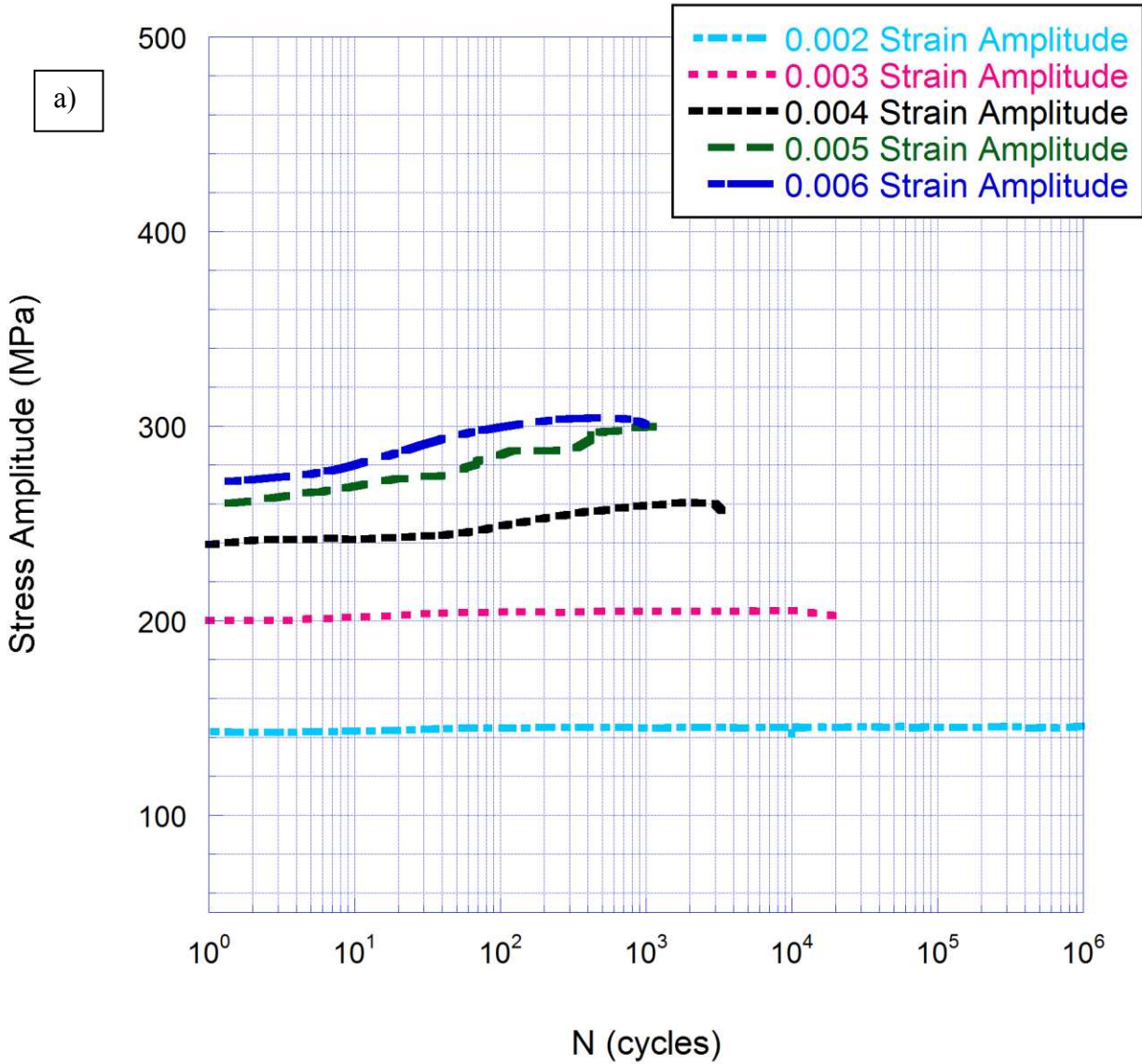


**Figure 8.** Stress-amplitude evolution over the cycle of the fatigue test for a) 6061-T6, b) 6061-A, c) 7075-T651, and d) 7075-A aluminum alloys.

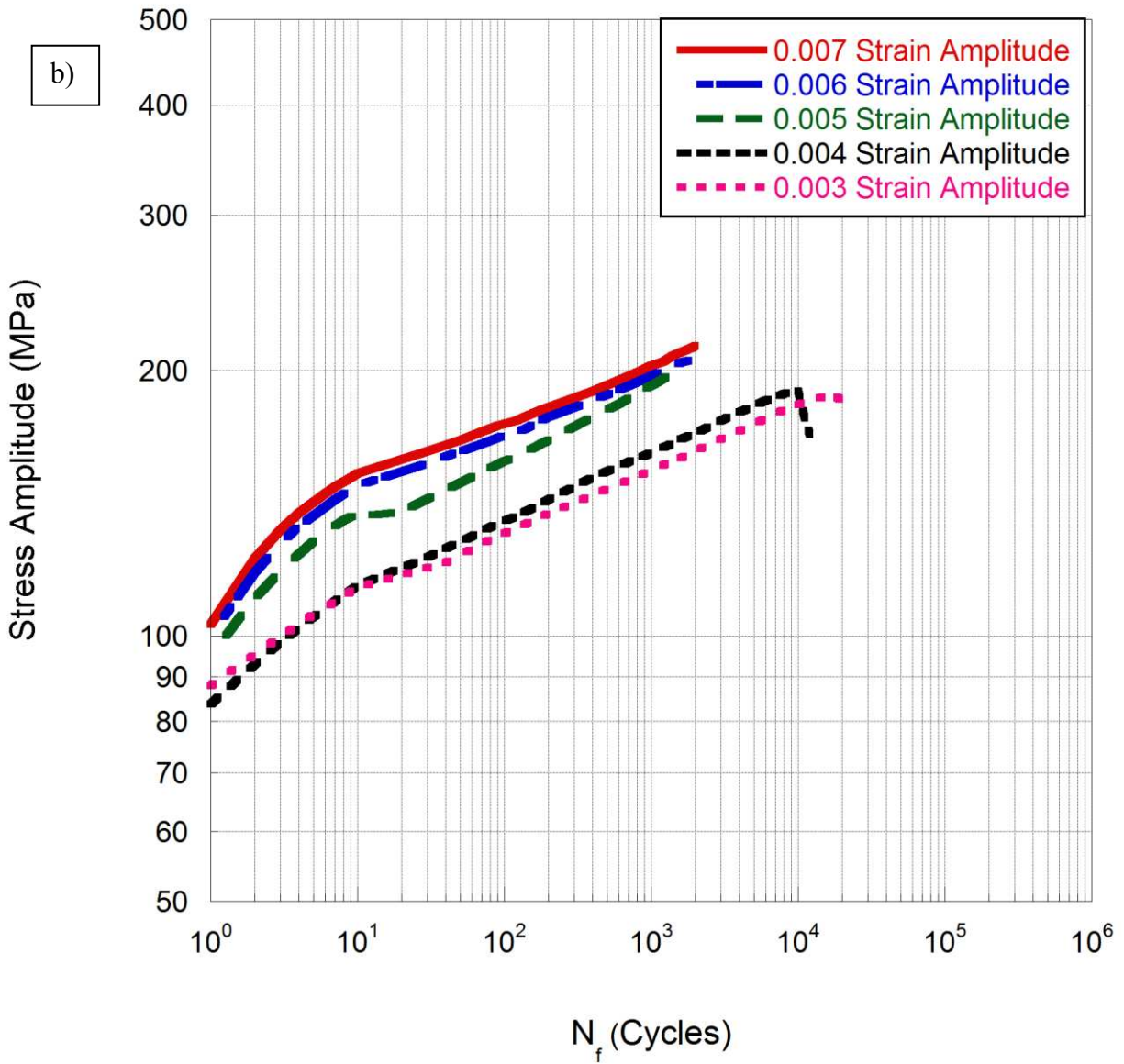


**Figure 8.** Stress-amplitude evolution over the cycle of the fatigue test for a) 6061-T6, b) 6061-A, c) 7075-T651, and d) 7075-A aluminum alloys (continuing).

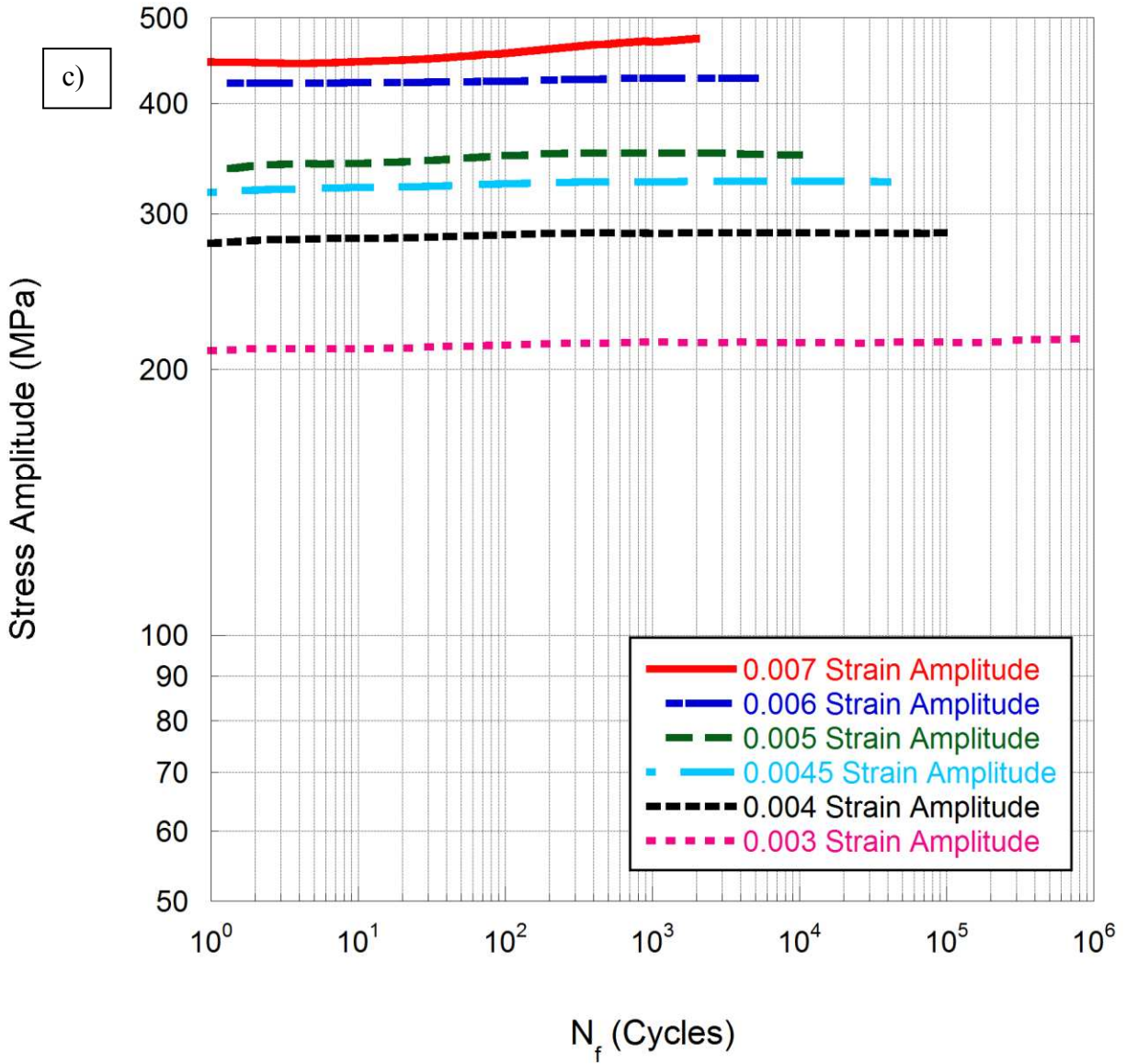


**Figure 8.** Stress-amplitude evolution over the cycle of the fatigue test for a) 6061-T6, b) 6061-A, c) 7075-T651, and d) 7075-A aluminum alloys (continuing).

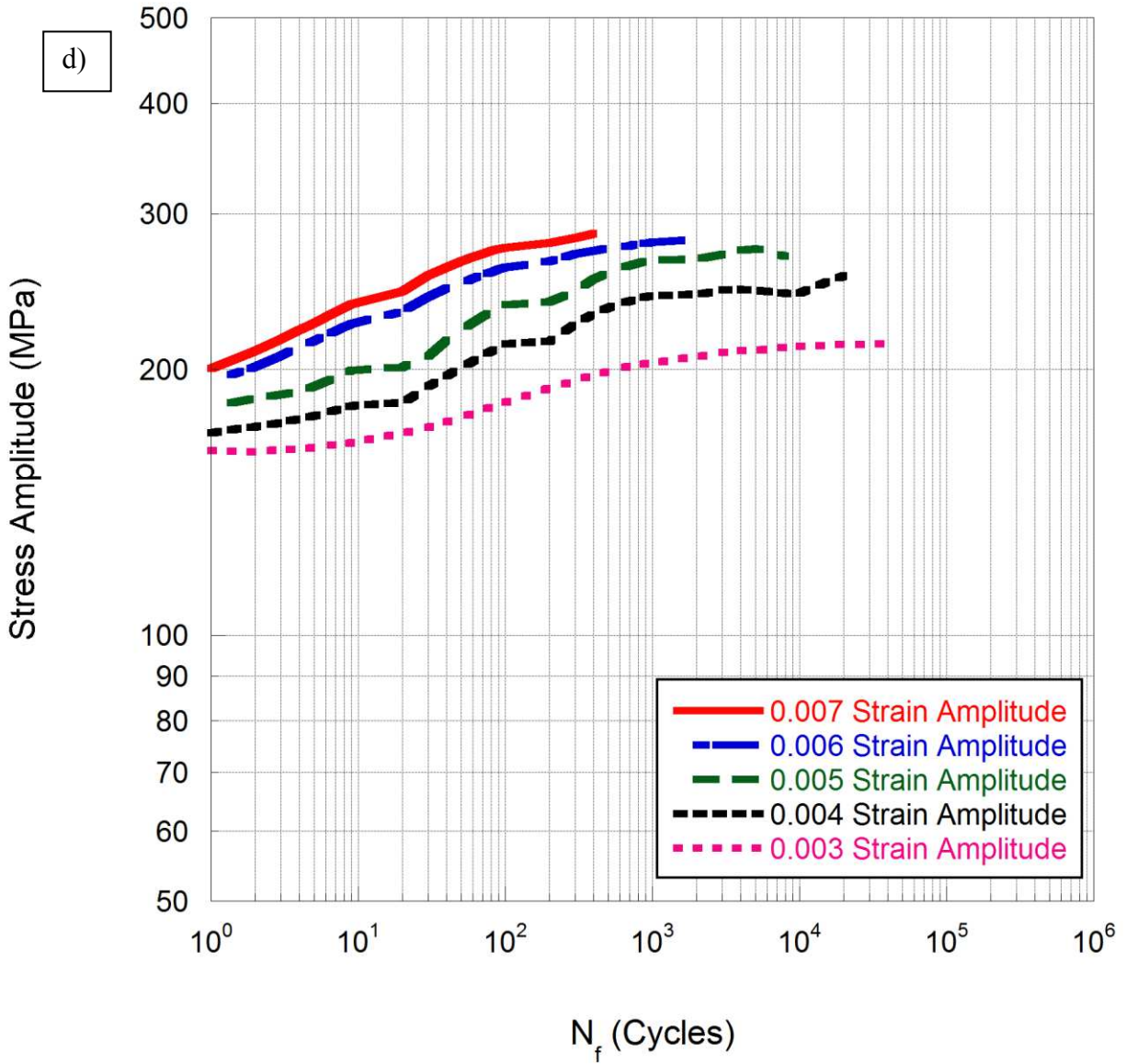


**Figure 8.** Stress-amplitude evolution over the cycle of the fatigue test for a) 6061-T6, b) 6061-A, c) 7075-T651, and d) 7075-A aluminum alloys (continuing).

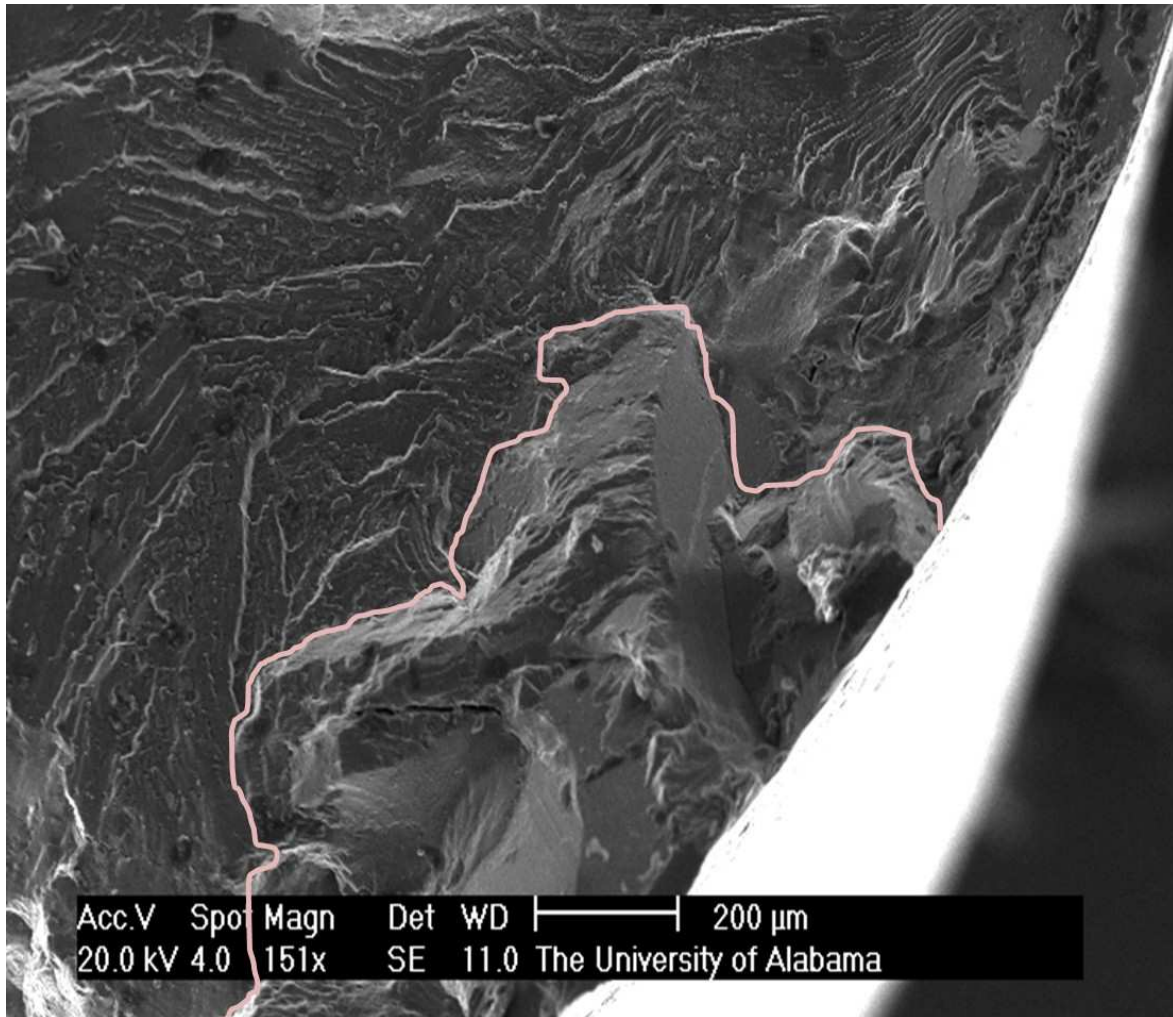


**Figure 9.** The particle in the image of specimen T-6-5, tested at 0.003 strain amplitude, is typical of the crack initiation sites found in the 6061-T6 aluminum alloy.

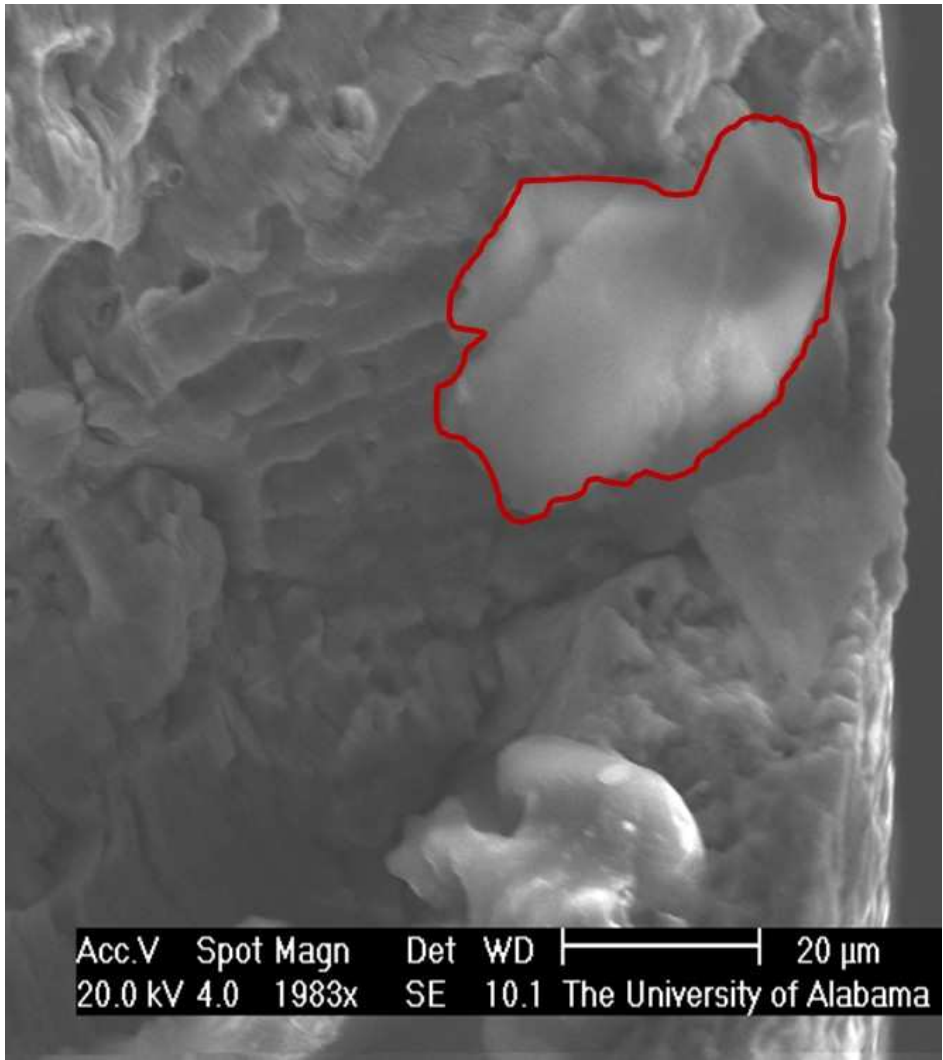


**Figure 10.** The particle in this image of specimen A-6-10, tested at 0.007 strain amplitude is typical of the crack initiation sites in the 6061-A aluminum alloy, with clusters of particles that are larger than those found in the 6061-T6 aluminum alloy.

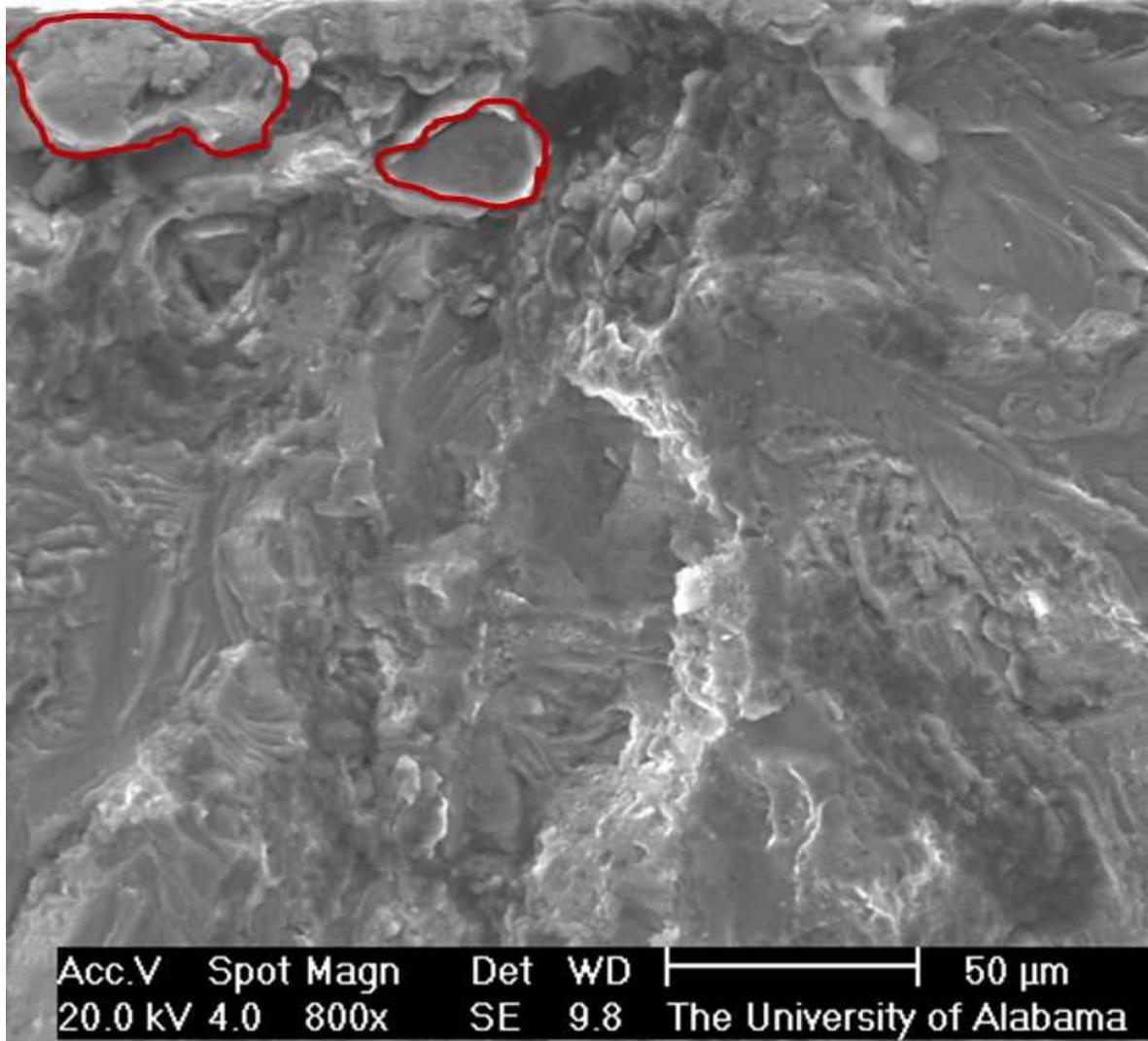


**Figure 11.** The particle in this image of specimen T-7-20, tested at 0.0045 strain amplitude is indicative of the initiation sites of 7075-T651 aluminum alloy. Almost exclusively the failures occurred at particle clusters.

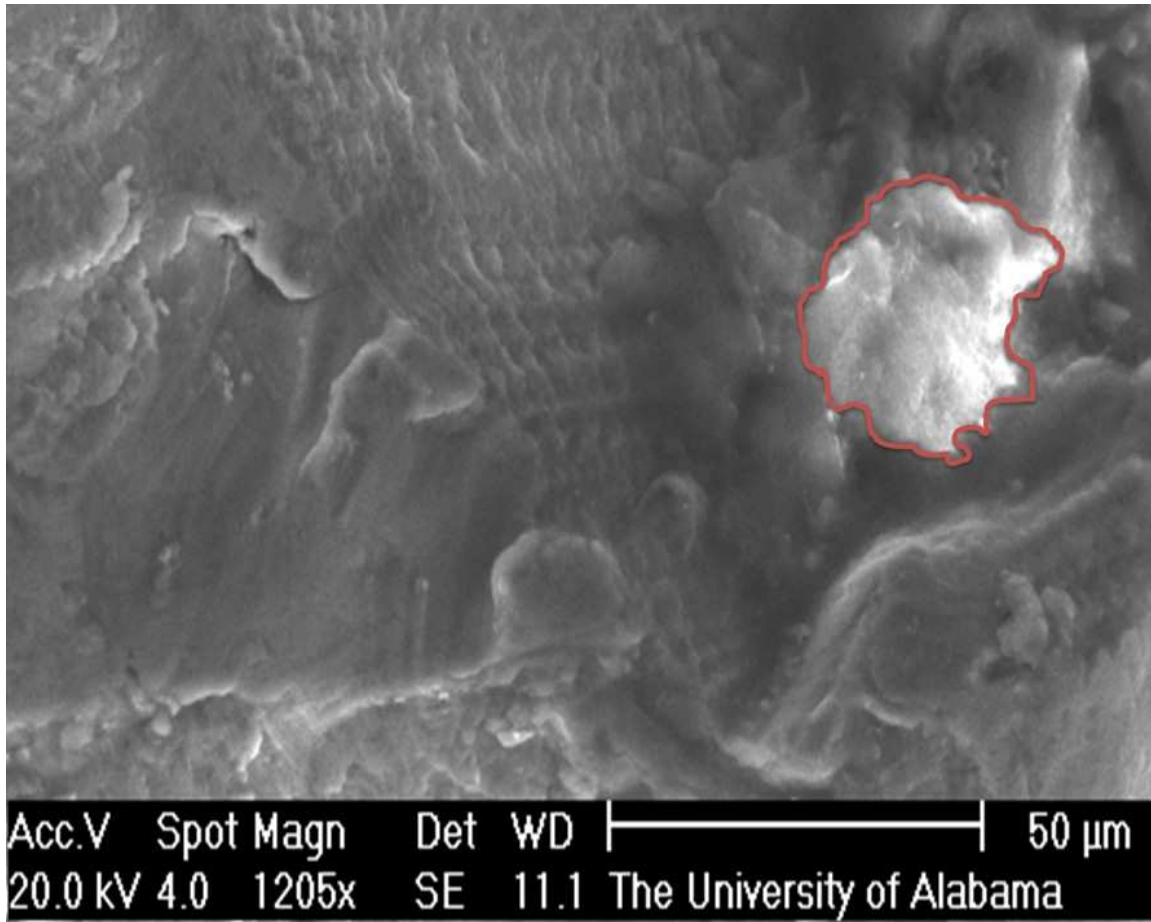


**Figure 12.** The particle in this image of specimen A-7-1 tested at 0.007 strain amplitude is one of the typical modes of failure.

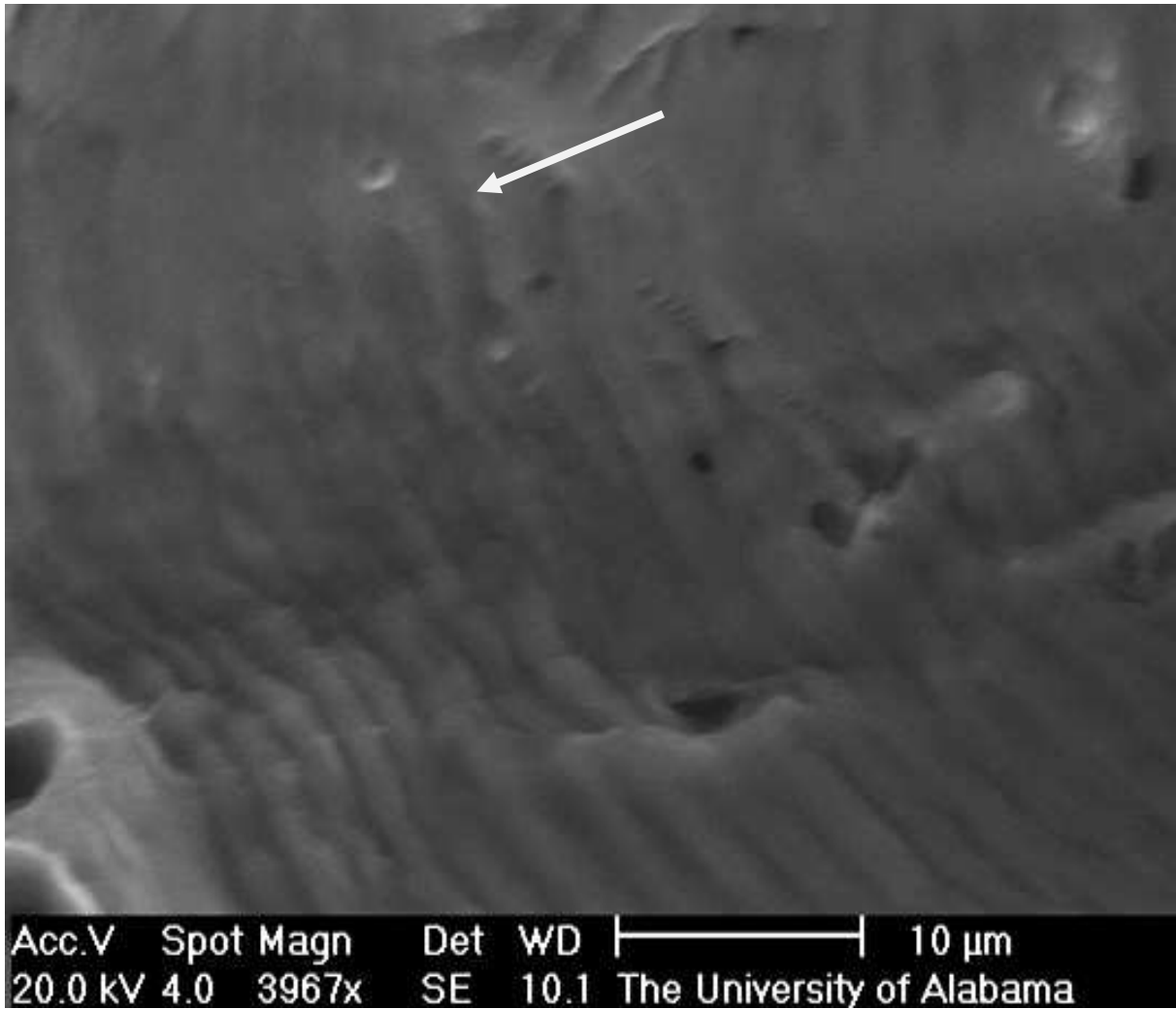


**Figure 13.** Fatigue striations were seen on most fracture surfaces on all materials represented by these shown from specimen A-6-8, with the crack growth direction indicated by the arrow.

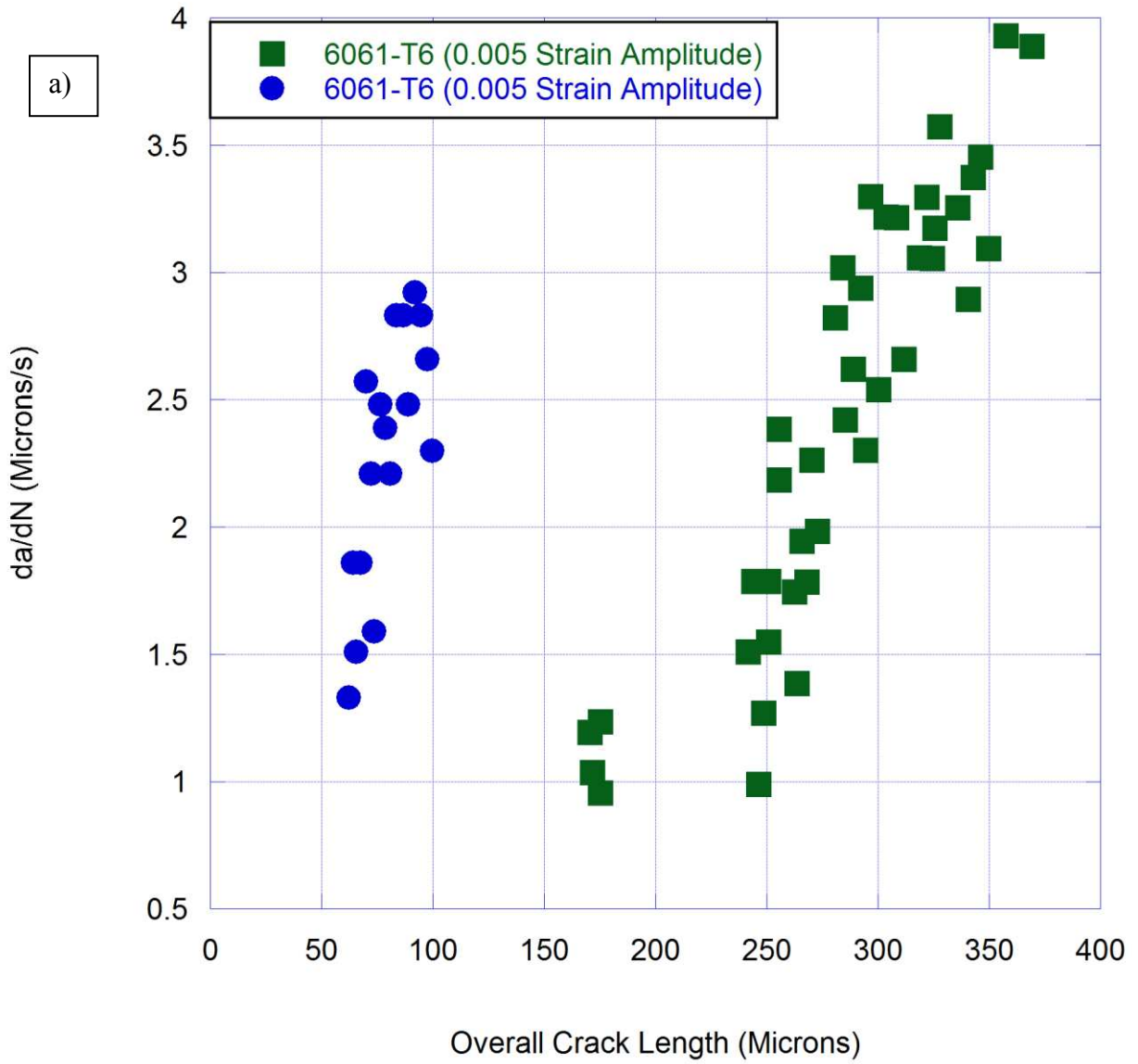


**Figure 14.** Compiled crack growth rates respective to overall crack length for a) the 6061 aluminum alloy and b) the 7075 aluminum alloy.



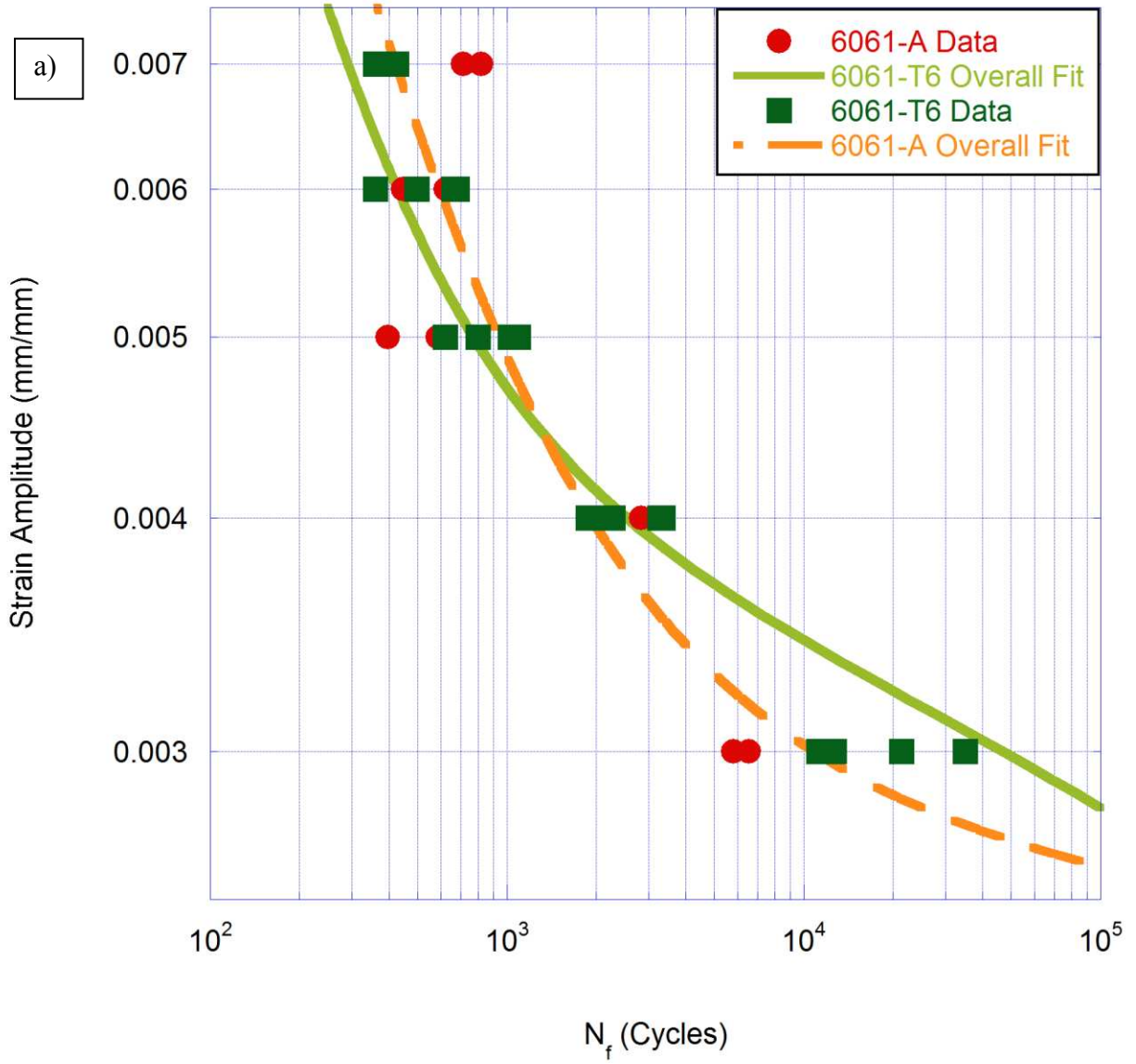


**Figure 15.** MSF model fit to the strain-controlled fatigue data in the peak-aged and heat-effected states for a) 6061 and b) 7075 aluminum alloys.

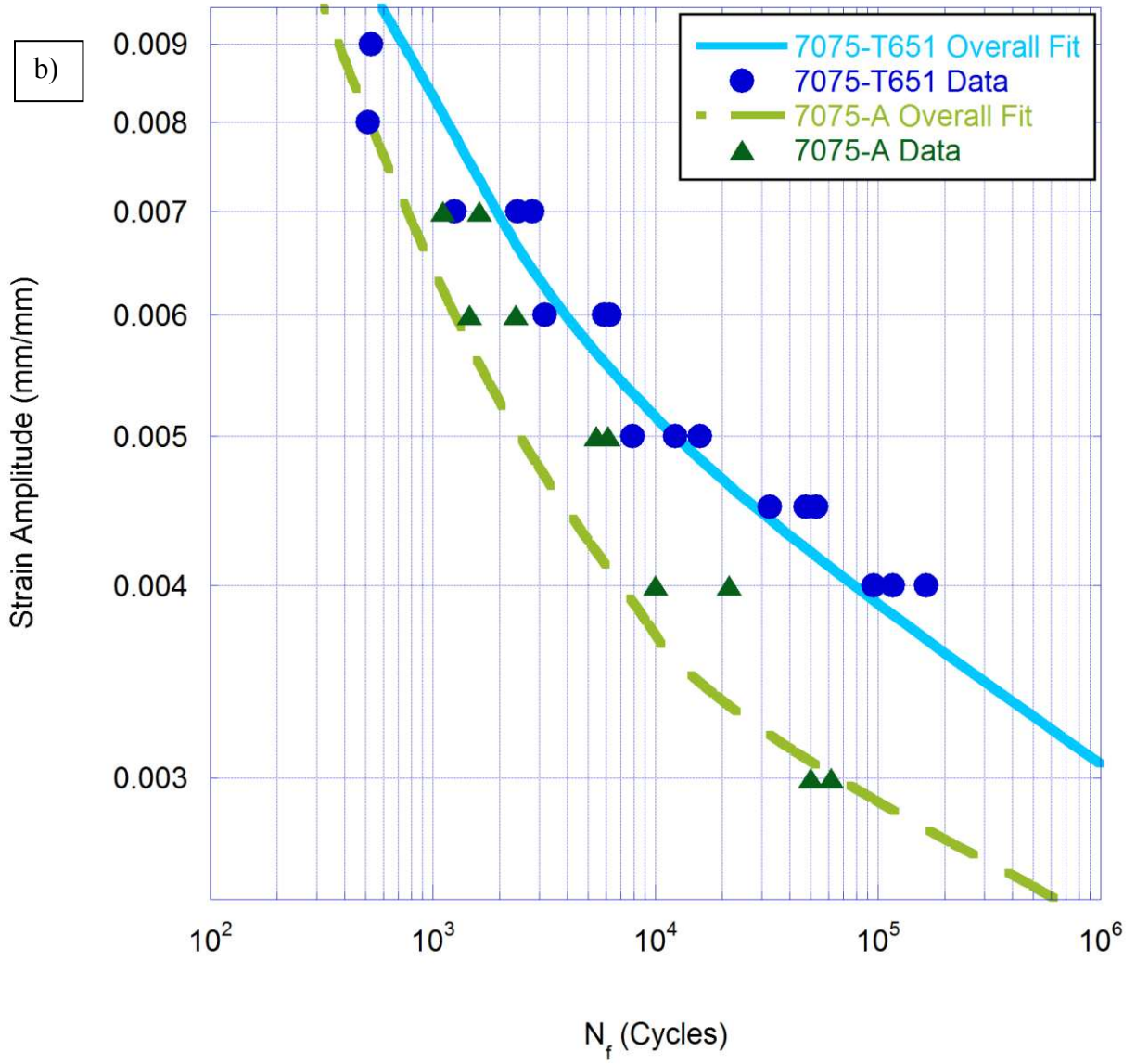


**Figure 15.** MSF model fit to the strain-controlled fatigue data in the peak-aged and heat-effected states for a) 6061 and b) 7075 aluminum alloys (continuing).

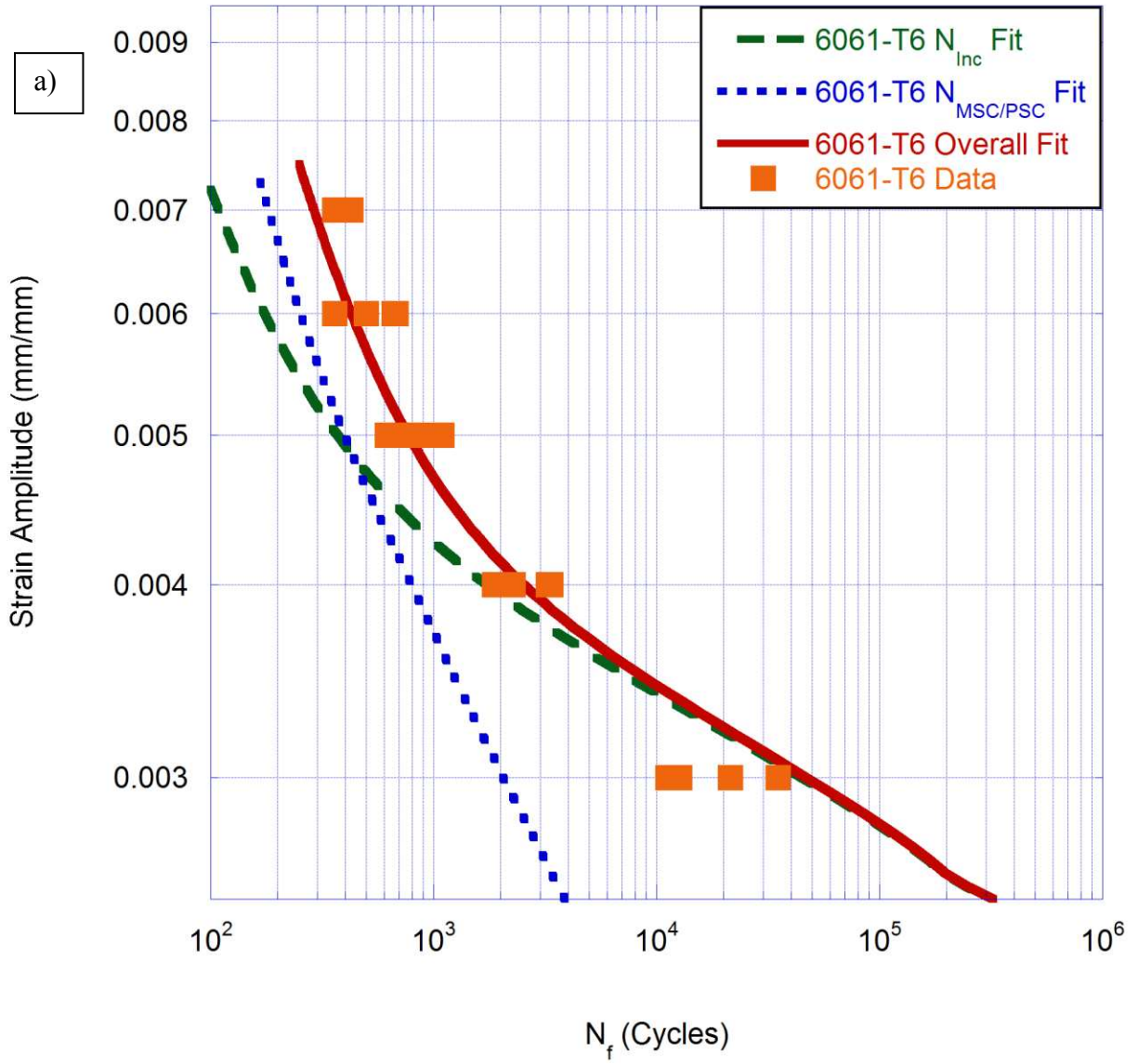


**Figure 16.** MSF fit of incubation and small crack growth for a) 6061-T6, b) 6061-A, c) 7075-T651, and d) 7075-A aluminum alloys.

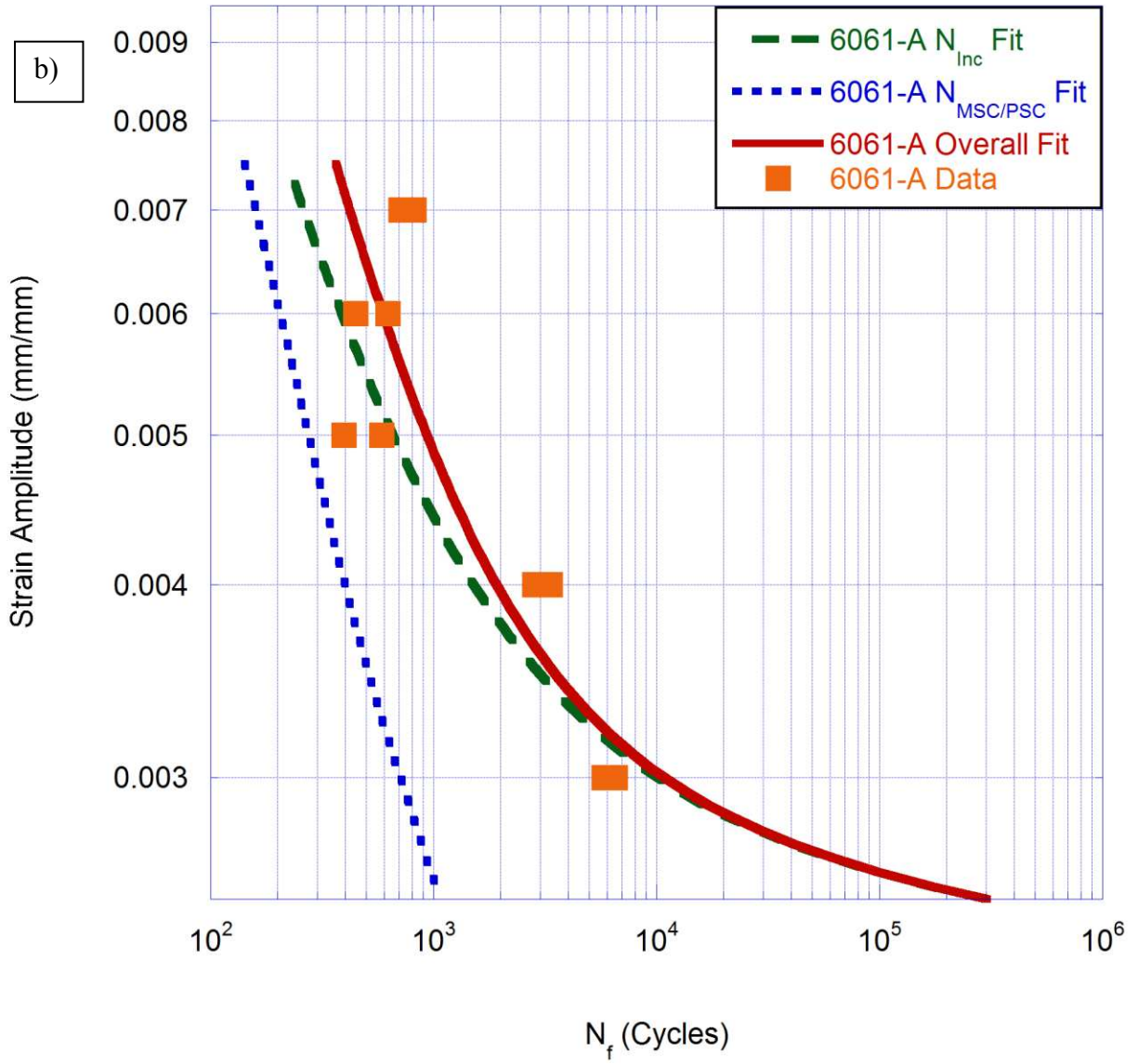


**Figure 16.** MSF fit of incubation and small crack growth for a) 6061-T6, b) 6061-A, c) 7075-T651, and d) 7075-A aluminum alloys (continuing).



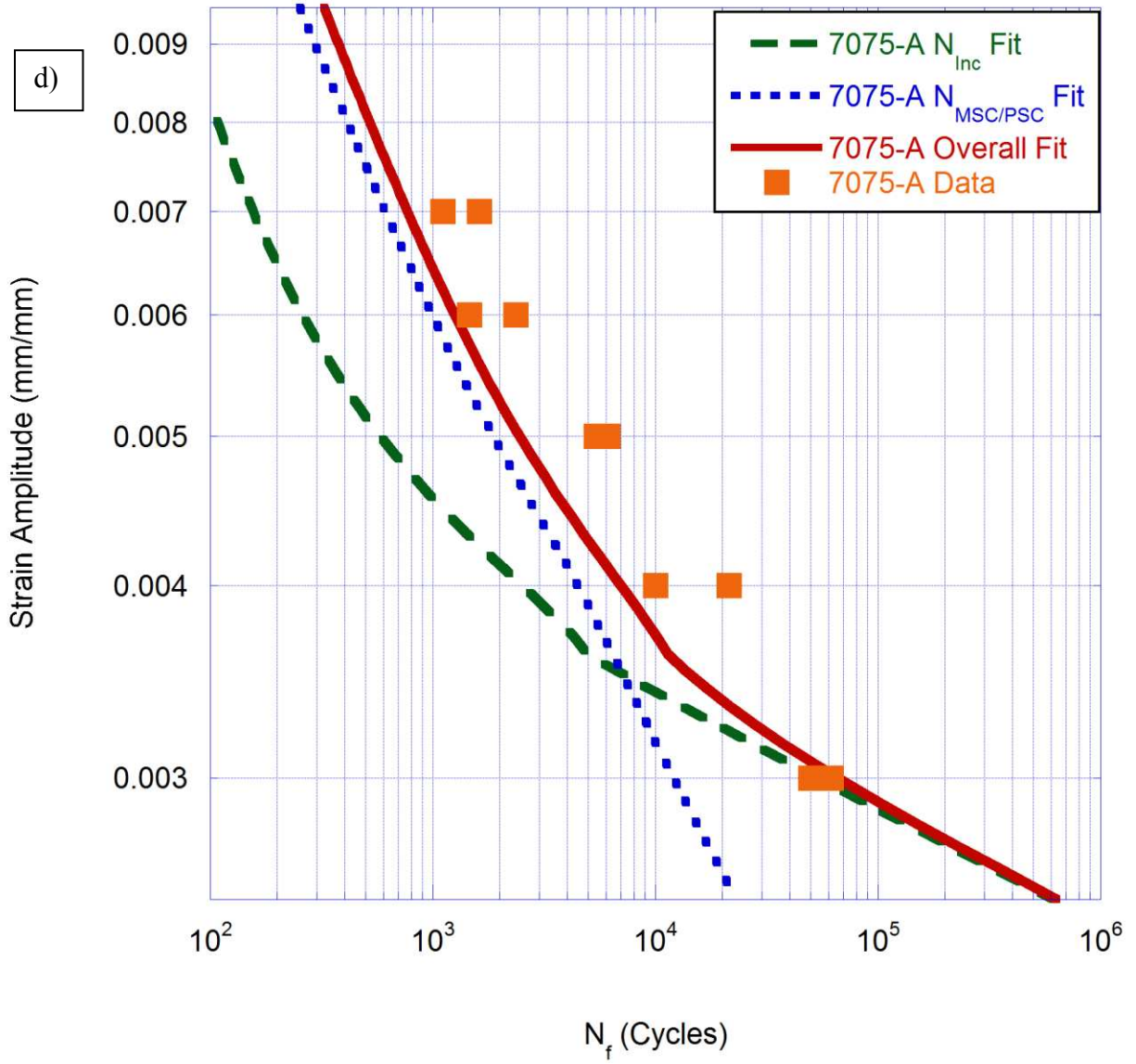


**Figure 16.** MSF fit of incubation and small crack growth for a) 6061-T6, b) 6061-A, c) 7075-T651, and d) 7075-A aluminum alloys (continuing).